

POLITECNICO DI TORINO  
Repository ISTITUZIONALE

CWE study of wind flow around railways: Effects of embankment and track system on sand sedimentation

*Original*

CWE study of wind flow around railways: Effects of embankment and track system on sand sedimentation / Horvat, Marko; Bruno, Luca; Khris, Sami. - In: JOURNAL OF WIND ENGINEERING AND INDUSTRIAL AERODYNAMICS. - ISSN 0167-6105. - ELETTRONICO. - 208:(2021), p. 104476. [10.1016/j.jweia.2020.104476]

*Availability:*

This version is available at: 11583/2855891 since: 2020-12-10T13:05:57Z

*Publisher:*

Elsevier

*Published*

DOI:10.1016/j.jweia.2020.104476

*Terms of use:*

This article is made available under terms and conditions as specified in the corresponding bibliographic description in the repository

*Publisher copyright*

(Article begins on next page)



## CWE study of wind flow around railways: Effects of embankment and track system on sand sedimentation

Marko Horvat <sup>a,\*</sup>, Luca Bruno <sup>a,c</sup>, Sami Khris <sup>b,c</sup>

<sup>a</sup> Politecnico di Torino, Department of Architecture and Design, Viale Mattioli 39, I-10125, Torino, Italy

<sup>b</sup> Optiflow Company, 160, Chemin de la Madrague-Ville, F-13015, Marseille, France

<sup>c</sup> Windblown Sand Modelling and Mitigation Joint Research Group, Italy



### ARTICLE INFO

#### Keywords:

windblown Sand  
Sedimentation  
Erosion  
Railway aerodynamics  
Embankment  
Track system  
Computational wind engineering

### ABSTRACT

Desert railways are constantly exposed to incoming sand blown by the wind. The railway body acts as an obstacle that perturbs the wind flow and the sand drift, resulting in zones of sand sedimentation and erosion. The insight into the local flow around the railway track and resulting sedimentation patterns is a necessary prerequisite to predict and prevent sand-induced limit states. The present study generally aims at filling such a gap, by investigating the local flow and the related potential sedimentation patterns around railways. The knowledge acquired about such patterns is required in the perspective of the design of innovative on-track Receiver Sand Mitigation Measures. The study adopts a Computational Wind Engineering approach to simulate the local wind flow, to obtain the shear stress field at the ground, to derive from it sand sedimentation/erosion patterns, and to obtain bulk performance metrics. The performances of different railway substructures and track systems are discussed under different incoming wind speeds and yaw angles. The simulated sedimentation/erosion patterns qualitatively agree with the field evidences observed along desert railways. The comparative analysis shows that rails elevated by humped sleepers or slab on top of a gentle-sloped substructure perform better than other track systems.

### 1. Introduction

Desert railways are exposed to the incoming wind flow, and wind-blown sand drift (Bruno et al., 2018b), as well as other man-built structures and infrastructures (Raffaele and Bruno, 2019). Windblown sand sedimentation and erosion occur in turn around them. In particular, accumulated sand causes a number of issues to railways ranging from Sand Serviceability Limit States (SSLS) to Sand Ultimate Limit States (SULS), as defined first in Bruno et al. (2018b).

Effective windblown Sand Mitigation Measures (SMMs) are mandatory to avoid the whole railway or one of its components to attain one of the Sand Limit States. SMMs have been recently categorized by Bruno et al. (2018b) with respect to the sand course and their working principles: Source SMMs are directly located on the sand source (dunes or loose sand sheets), and intended to prevent erosion; Path SMMs are deployed along the windblown sand path ranging from the sand source to the infrastructure, and aim at inducing sedimentation; Receiver SMMs are directly located on the infrastructure, and conceived to avoid sedimentation.

Bruno et al. (2018b) have also reviewed the Receiver SMMs proposed so far in literature. Jet roofs and artificial tunnels are large and costly SMMs intended to fully shelter the track and promote the sand flying over it. Sand-resistant solutions include ballastless track systems, obviously capable of avoiding sand-induced ballast contamination. Among them, the Tubular-Track® system was tested along KSA and Namibian railway deserts (van der Merwe, 2013), and the Rheda 2000® slab system was installed along the Medina-Mecca high speed line (Merino, 2014). Other track systems aim at promoting sand erosion. Among them, the so-called humped sleepers (Riessberger and Swanepoel, 2005; Zakeri et al., 2012; Riessberger, 2015; Reissberger et al., 2016) are conceived to take advantage from the Venturi effect. The humps elevate rails over the ballast surface, potentially allow free passage of accelerated wind-flow underneath, involve high wall shear stresses beneath the rail, and finally induce local erosion. Recently, Moyan et al. (2020) tested an analogous solution, where gaps under the rails are achieved by removing portions of ballast between successive standard sleepers. The humped slab tracks combine humps and ballastless systems (Zakeri et al., 2011). They have been tested in situ along short segments of the Namibian

\* Corresponding author.

E-mail address: [marko.horvat@polito.it](mailto:marko.horvat@polito.it) (M. Horvat).

(Riessberger and Swanepoel, 2005) and the Iranian railways (Zakeri, 2012).

While the efficiency of Source and Path SMMs is irrespective and independent of the local wind flow around the railway, the conceptual design of innovative aerodynamic-based on-track Receiver SMMs cannot disregard the aerodynamic behavior of the unmitigated railway, and the mapping of sand sedimentation patterns along it. As a matter of principle, the whole railway system aerodynamics result from the combined effects of the railway substructure and superstructure, and from their interaction, if any. In this perspective, the *substructure* is treated herein as the grouping of embankment and ballast bed, if any, that resolves into an overall ridge with stepped inclined slopes. The *superstructure* is the ensemble of the track system components that rest on the substructure, such as sleepers or slab, and rails.

The *substructure aerodynamics* shares some common flow features with nominally two dimensional *fundamental landforms*, such as trapezoidal ridges, ideal transverse dunes, sloped escarpments and forward-facing step as a limiting case of the latter. The flow around these forms has been widely studied since the end of Seventies by Wind Tunnel (WT) tests (Bowen and Lindley, 1977; Bowen, 1983; Shiao and Hsieh, 2002), and later by Computational Wind Engineering (CWE) simulations (Deaves, 1980; Paterson and Holmes, 1993; Smyth, 2016). Taken as a whole, such studies testify the wind flow along the top surface of the form depends on the inclination of the upwind slope and on the height of the form with respect to the incoming wind speed profile. The first attempts in geomorphology sciences, especially the ones addressed to relate the wind flow and the morphodynamic of such basic forms, are by far more recent. The aerodynamics of ideal transverse dunes has been widely studied in the recent past both experimentally and computationally (see e.g. Liu et al., 2011; Bruno and Fransos, 2015, and cited references therein). Hesp and Smyth (2019) provide a detailed overview of previous studies on escarpment aerodynamic in geomorphological literature, complemented by some references in fluid dynamics.

Several studies explicitly refer to *railway substructures*. Most of them are mainly focused on train aerodynamics under cross wind: let us cite the WT tests by Baker (1986), Suzuki et al. (2003) and Schober et al. (2010), the systematic WT campaign by Boccilone et al. (2008); Cheli et al. (2010); Tomasini et al. (2014), the computational simulations by Zhang et al. (1995) and Ishak et al. (2019), the hybrid WT-CWE coupled approach by Diedrichs et al. (2007) and Noguchi et al. (2019). A single study (Zhang et al., 2019) simulates the wind flow around the substructure to ground the design of in-situ anemometric monitoring layout. Some other studies specifically address the wind-induced erosion of the embankment, i.e. the WT tests by Boyin et al. (1992), and the computational simulations by Zhang et al. (1995). Sand transport, erosion and sedimentation around the embankment are tentatively discussed by wind + sand tunnel test in Xiao et al. (2015) and two-phase CWE simulations in Moyan et al. (2020).

The results of the studies above depend on the field of application and related objectives. The studies in train aerodynamics mainly discuss pressure and forces acting on the rolling stock, the embankment being included as a scenario which can affect the train aerodynamics. A limited number of such studies directly investigate the local flow around the substructure without train model: Cheli et al. (2010) provide anemometric measurements of the speed-up ratio for different yaw angle; Noguchi et al. (2019) analyze in deep the velocity field of the simulated flow under two yaw angles, and in particular discuss the conditions under which the Prandtl's independence principle holds in the wake of experimental evidence in Baker (1985, 1986). Zhang et al. (2019) provide a detailed analysis of both the instantaneous and time-averaged flow quantities around the whole double-track. The aerodynamic studies about wind-induced erosion and sedimentation are ultimately and specifically interested in the distribution of the wind shear stress at the embankment surface, and to compare it with the threshold value above which erosion takes place (Bagnold, 1941; Raffaele et al., 2016, and cited references). The measurement of such a state variables is challenging in

WT tests: the early study by Boyin et al. (1992) is limited to providing the pressure coefficient distribution and the mean wind velocity; the recent paper by Xiao et al. (2015) includes the wind velocity field along simplified substructure geometry. Conversely, the shear stress field is easily postprocessed from CWE simulations: the paper by Zhang et al. (1995) complements the pressure coefficient distribution with the streamline field visualization and the shear stress distribution at different Re numbers. Surprisingly, Moyan et al. (2020) do not provide the shear stress distribution along the adopted single track with a quite unconventional embankment.

On the one hand, the *experimental setup and computational models* are adapted to application field and flow quantities of interest. In particular, computational models adopted for train aerodynamics and monitoring layout aim at capturing the instantaneous flow features and aerodynamic forces besides the time-averaged ones, e.g. in Noguchi et al. (2019), Zhang et al. (2019), Diedrichs et al. (2007) and Ishak et al. (2019). Conversely, computational studies devoted to erosion and sedimentation are interested in the time-averaged flow features responsible for the long-term morphodynamics of the sand surface: in the light of this, both Zhang et al. (1995) and Moyan et al. (2020) adopt a steady RANS approach. On the other hand, minimum requirements should be respected by WT tests and CWE simulations to guarantee basic similarity requirements regardless of the study specific goals. Among them, the geometric similarity of the substructure and the extension of the experimental/computational domain are of paramount importance.

The *superstructure aerodynamics* is overlooked in literature. Its effects on train aerodynamics are probably negligible, but it is expected that they play a prominent role in windblown sand erosion/sedimentation along the track, and the knowledge gained from the flow around the superstructure to be a relevant background for the design of receiver SMMs. This lack of knowledge follows from the multiscale features of the resulting modelling problem: rails and other track components have a characteristic spatial scale (dozen of cm) that differ by two orders of magnitude from the characteristic scale of the substructure. It follows that simplified rails are included only in the largest scale models of few WT tests, e.g. Cheli et al. (2010); Tomasini et al. (2014); Noguchi et al. (2019), but their similarity requirements and aerodynamic effects are not discussed. The very most of CWE models do not include any component of the track system (Zhang et al., 1995, 2019; Noguchi et al., 2019; Ishak et al., 2019), because of the high number of cells resulting from the spatial discretization around them, and the significant computational cost of the simulations in turn. Only Moyan et al. (2020) very recently made an attempt to account for rails in their computational model, in order to evaluate the effects on the wind-sand flow of gaps obtained by removing the upper part of the ballast bed between successive sleepers. In order to reduce the computational cost, Moyan et al. (2020) model the intrinsically 3D flow around the track by using two 2D domains in the vertical planes at the midpoints between two successive sleepers and two successive gaps. Such an approach is clearly ill-posed in aerodynamic terms, i.e. the width of gaps and sleepers in the railway direction is close to the rail and gap height, so that nominally 2D flow cannot develop along the rail direction.

In the light of the above state of art, two main shortages in literature can be outlined: i. the effects of the components of the superstructure, and their aerodynamic interaction with the substructure, are completely overlooked; ii. the wind-induced shear stress around the railway are not measured or reported nor discussed, in spite of its dramatic effect on windblown sand sedimentation and erosion. The general goal of the study is to fill the gap in the lack of knowledge concerning the railway aerodynamics in the perspective of the design of innovative on-track Receiver SMMs. In particular, the aerodynamic effects of the geometry of the substructure, of different track systems, and of the yaw angle are obtained by computational simulations. Results are discussed in terms of both flow structures around the railway, and potential sand sedimentation patterns on its surface.

To achieve the goal, the paper develops in five further sections.

Section 2 collects field evidence of sand sedimentation patterns along railways, and infers causes by their morphological qualitative reading. Section 3 summarizes the wind flow modeling and adopted computational approach. Section 4 details the considered setups, in terms of incoming flow features and geometries of both the substructure and superstructure. The findings of the study are critically discussed in Section 5: the effects of substructure, superstructure and yaw angle on both the global flow around the whole railway and local flow around the track are detailed in separate subsections. Finally, conclusions and perspectives are outlined in Section 6.

## 2. Field evidence of sand sedimentation patterns

A selection of sand sedimentation patterns along railways is shown in Fig. 1. They were observed during site visits along railways in Iran (Bam - Zahedan line, Fig. 1b, c, f), Algeria (Redjem Demouche - Mecheria line, Fig. 1d, e, g), and Namibia (Aus - Lüderitz line, Fig. 1a, h, j, Swakopmund - Walvis Bay line, Fig. 1i taken from Riessberger, 2015).

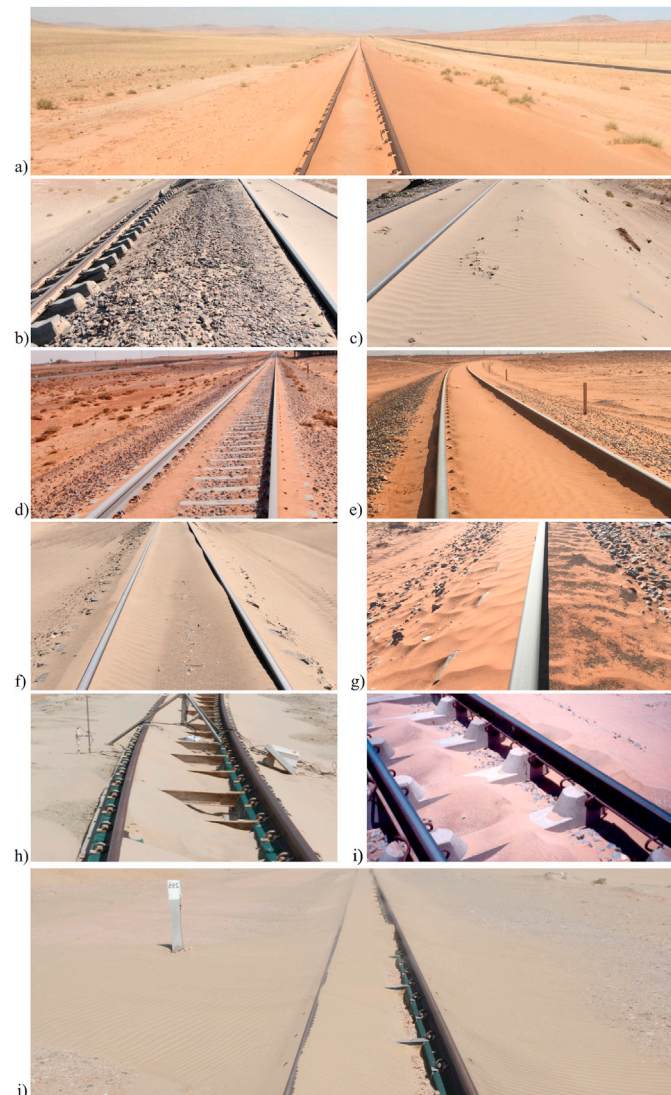


**Fig. 1.** Observed sand sedimentation patterns around railways. General patterns around the railway (a) and the substructure (b, c). Local Patterns around standard railway system (d, e). Different granulometry of sedimenting particles (f, g). Local patterns around non-conventional track systems (h,i). Pattern due to yawed incoming wind (j). Inferred prevailing wind directions from left to right in all pictures. Photocredits: pictures a, h, j - C. Nash and G. Wiggs, University of Oxford, SMaRT members; pictures b, c, f - F. Genta, Astaldi Company, SMaRT partner organization; pictures d, e, g - M. Horvat, C. Nash and R. Nuca, SMaRT early stage researchers; picture i - [Riessberger \(2015\)](#), with the permission to reuse under a Creative Commons Attribution License.

Zahedan line, Fig. 1b, c, f), Algeria (Redjem Demouche - Mecheria line, Fig. 1d, e, g), and Namibia (Aus - Lüderitz line, Fig. 1a, h, j, Swakopmund - Walvis Bay line, Fig. 1i taken from Riessberger, 2015).

First, their morphological reading allows to preliminary categorize recurrent sedimentation scenarios, tentatively recognize the incoming wind and railway geometrical features that affect them, and drive selection of the setups for computational simulations. Second, the local wind conditions which caused them can be qualitatively inferred, although observed sedimentation patterns are not systematically accompanied by in-situ anemometric measurements of the wind speed. Indeed, there is a chain relation among the wind velocity gradient  $\partial U/\partial n$  along the boundary layer thickness, the wind induced shear stresses at the ground surface  $\tau \propto \partial U/\partial n|_{n=0}$ , the shear stress threshold value  $\tau_t \propto d$  that separates grain sedimentation ( $-1 = \tau/\tau_t \leq +1$ ) and erosion conditions (windward erosion for  $\tau/\tau_t > +1$ , backward erosion for  $\tau/\tau_t < -1$  induced by reversed flow), where  $d$  is the sand diameter.

*Global sedimentation pattern* around the whole railway is shown in Fig. 1(a). Across the far field around the railway the windblown sand transport takes place at equilibrium, and the ground surface is sand-free. Conversely, close to the railway its body acts as a ground-mounted obstacle, locally disturbs the wind velocity profile, non equilibrium conditions rise and sedimentation or erosion prevail. A sandy corridor along the railway results across the vegetated land. In some sense, the railway causes its own sand troubles.

*Sedimentation around the substructure* is exemplified in Fig. 1 (b) and (c), where the same railway segment is observed from upwind and downwind side, respectively. A typical asymmetric erosion and sedimentation pattern can be easily observed along the side slopes of the high-rise embankment: the upwind one is in prevailing erosion regime, because of the flow speedup; conversely, downwind slope is fully covered by sedimented sand, because it lies in the reversed flow region characterized by lower kinetic energy. In this case the upwind rail acts as a sharp watershed between erosion and sedimentation, i.e. its head is supposed to induce the massive boundary layer separation. This separation mode cannot be generalized, because other features are expected to affect it, e.g. the height and edge roundness of the embankment and ballast bed among others. However, it suggests that the global aerodynamics and morphodynamic can be affected by the local perturbations of the track components.

*Local sedimentation patterns around a standard ballasted track system* are detailed in Fig. 1 (d) and (e). Clear differences can be observed between them and the previous case with regard to the local sedimentation around rails and along the gauge. In particular, sand sedimentation occurs upwind the upwind rail in 1 (d)-(e), while the same does not hold in 1 (b). Such a difference could be ascribed to the effects of the low-rise embankment and sharp edges of the ballast bed, among other causes. This suggests that the local aerodynamics and morphodynamic are affected by the global perturbations of the substructure. In summary, the strong coupling between local and global phenomena is conjectured. Furthermore, the two local patterns in Fig. 1 (d)-(e) are different, even though they occur on the same geometry and for the same sand granulometry. In particular, the gauge is partially sand-free in 1 (d), while a thin and quasi uniform sand layer occurs in 1 (e). We conjecture that such differences can partially occur due to different incoming wind speeds and related values of the wall shear stress  $\tau$ . In addition, Fig. 1 (f) and (g) shed some light on natural segregation of grains with different diameters or of sand and organic particles around the upwind rail. Clear sorting between fine white sand and coarser gray sand can be seen in Fig. 1 (e); in Figure (f) organic particles with lower density sediment in different area than the rest of the sand. Such field evidences clearly confirm that particle diameter, density, and consequently  $\tau_t$  significantly affect the sedimentation patterns.

*Local sedimentation patterns around non-conventional track systems* are shown in Fig. 1 (h) and (i). Fig. 1 (h) refers to Tubular-Track system (T-Track®): a large amounts of sand is unintentionally trapped within the gauge, notably downwind the upwind rail. This phenomenon is

suspected to be triggered by the high continuous concrete beams on which rails are mounted, and induced massive boundary layer separation. Fig. 1 (i) refers to non-conventional humped sleepers. The sand-free ballast surface below the rails confirms the desired Venturi effect locally takes place, the wind flow is accelerated through the gaps, and erosion results. However, undesired sedimentation occurs along the mid part of the gauge in form of sand piles. We conjecture this is due to the jet-flow expansion and deceleration at the outlet of the upwind gap.

A local sedimentation pattern under yawed incoming wind is shown in Fig. 1 (j). Incoming wind direction non orthogonal to the alignment is testified by the direction of the sand ripples upwind the railway. Ripples are also clearly visible along the gauge and downwind the track, but their direction differs from the upwind ones. This evidence suggests that railway causes the deflection of the local wind flow, analogously to what has been proven e.g. by Bauer et al. (2013) and Hesp et al. (2015) with reference to dunes and forward facing step, respectively. The sedimentation pattern under yawed wind in Fig. 1 (j) significantly differ in shape from the one under orthogonal wind (Fig. 1-h), although both patterns refer to the same substructure, track system and sand characteristics.

The ensemble of the field evidences discussed above confirms the huge variety of sedimentation patterns. They are conjectured to mainly depend on the geometry of substructure and superstructure, speed and yaw angle of the incoming wind speed, sand diameter and related mechanical features. The effects of such parameters are systematically investigated in the following computational study.

### 3. Computational model

#### 3.1. Mathematical model

In the light of the state-of-art discussed in Sect. 1, a 3D steady RANS approach is adopted in this study. In fact, RANS approach is perfectly adapted to simulate the time-averaged flow features responsible for the long-term morphodynamics of sand dunes (e.g. in Liu et al., 2011; Araújo et al., 2013; Bruno and Fransos, 2015; Lima et al., 2017), and around railways (Zhang et al., 1995; Moyan et al., 2020). In particular, the SST  $k - \omega$  turbulence model is selected for the current application because of its proven accuracy in bluff-body aerodynamics in general (Menter, 1994; Menter et al., 2003), and for fundamental topographical forms (Bruno and Fransos, 2015) or windblown sand solid barriers (Bruno et al., 2018a; Horvat et al., 2020).

The whole set of governing equations in Einstein notation and cartesian coordinates reads:

$$\frac{\partial u_i}{\partial x_i} = 0, \quad (1)$$

$$u_j \frac{\partial u_i}{\partial x_j} = -\frac{1}{\rho} \frac{\partial p}{\partial x_i} + \frac{\partial}{\partial x_j} \left[ \nu + \nu_t \frac{\partial u_i}{\partial x_j} + \frac{\partial u_j}{\partial x_i} \right], \quad (2)$$

$$u_j \frac{\partial k}{\partial x_j} = \frac{\partial}{\partial x_j} \left[ (\sigma_k \nu_t + \nu) \frac{\partial k}{\partial x_j} \right] + \tilde{P}_k - \beta^* k \omega, \quad (3)$$

$$u_j \frac{\partial \omega}{\partial x_j} = \frac{\partial}{\partial x_j} \left[ (\sigma_\omega \nu_t + \nu) \frac{\partial \omega}{\partial x_j} \right] + C_{\omega_1} \frac{\omega}{k} P_k - C_{\omega_2} \omega^2 + (1 - F_1) \frac{2\sigma_{\omega_2}}{\omega} \frac{\partial k}{\partial x_i} \frac{\partial \omega}{\partial x_i}, \quad (4)$$

where  $u_i$  is the averaged velocity,  $p$  the averaged pressure,  $\rho$  the air density,  $\nu$  the air kinematic viscosity,  $k$  the turbulent kinetic energy,  $\omega$  its specific dissipation rate, and  $\nu_t = k/\omega$  the turbulent kinematic viscosity. The kinetic energy production term  $\tilde{P}_k$  is modeled by introducing a limiter to prevent the build-up of turbulence in stagnation regions:

$$\tilde{P}_k = \min(P_k, 10\beta^* k \omega), \quad \text{where } P_k \approx \nu_t \frac{\partial u_i}{\partial x_j} + \frac{\partial u_j}{\partial x_i} \frac{\partial u_i}{\partial x_j}.$$

For the sake of conciseness, the definition of the blending function  $F_1$  and the values of the model main constants  $\beta^*$ ,  $\sigma_k$ ,  $\sigma_\omega$ ,  $C_{\omega_1}$  and  $C_{\omega_2}$  are omitted herein. Interested readers can find them in Menter et al. (2003).

Near the wall, the SST  $k - \omega$  model is complemented by the so-called sand-grain roughness wall functions. They are selected for the current application because of their wide use in environmental CWE in general (e.g. Blocken et al., 2007) and the proofs of adequacy obtained in previous 3D simulations of sand dune aerodynamics by Liu et al. (2011); Jackson et al. (2011, 2013); Bruno and Fransos (2015). In particular, standard wall functions (Lauder and Spalding, 1974) with roughness modification (Cebeci and Bradshaw, 1977) are applied. The equivalent sand-grain roughness height is determined as  $k_s = 9.793z_0/C_s$ , where  $C_s = 0.5$  is the roughness constant and  $z_0$  is the aerodynamic roughness length.

The adopted 3D computational domain is shown in Fig. 2 (b). The domain includes flat ground both upwind and downwind the railway, and the railway itself.

The origin of the coordinate system is set at the far field ground level, positioned so that the  $y - z$  vertical plane includes the railway longitudinal axis. The railway is arranged in the domain so that its longitudinal axis is normal to the domain lateral faces. The distance from the upwind foot of the embankment to the inlet boundary is equal to 25 times the overall height  $H$  of the railway above the ground level, while the one from the downwind foot of the embankment to the outlet boundary is 50H. The height of the domain is equal to 20H.

Such distances are set equal to or larger than the ones adopted in previous computational studies on analogous applications (e.g. Bruno and Fransos, 2015; Zhang et al., 2019; Noguchi et al., 2019), and are by far large enough to avoid influences of boundary conditions on the results. The trackwise size  $L_y = 10H$  is set in the wake of a preliminary study (see subsect 5.1).

No-slip boundary conditions (b.c.) are imposed at the solid walls. Neumann zero-gradient b.c. is imposed for all the flow variables at the top and outlet faces, except for Dirichlet b.c. for pressure at outlet. Periodic b.c. are applied at the domain side faces. The incoming upwind far-field is modeled by means of b.c. at the inlet face, and the related state variables indicated by the subscript 0. Neumann b.c. is used for pressure, while Dirichlet b.c. are imposed on  $u$ ,  $k$  and  $\omega$ . In particular, the profiles of  $k_0(z)$  and  $\omega_0(z)$  are set in accordance with Richards and Norris (2011) to replicate the neutral atmospheric boundary layer. The velocity profile is prescribed using the log-law  $u_0(z) = \frac{u^* \cdot 0}{\kappa} \log \left( \frac{z - z_0}{z_0} \right)$ , where  $\kappa = 0.41$  is the Von Kármán constant,  $u^* \cdot 0$  the shear velocity,  $z_0$  the aerodynamic roughness length. Such combination of velocity and turbulence is in equilibrium, ensuring that the specified profiles do not further develop in the domain (see subsect 5.1 for proof). Generally speaking, two approaches can be adopted to account for relative angle of attack between railway and incoming wind direction. In the first, the wind direction is kept constant while the railway is rotated around the vertical axis. Such an approach is commonly adopted in WT tests, and in some computational studies. Alternatively, the railway alignment is fixed in place, while the wind direction at inlet is varied. In this study, this second approach is chosen. The inlet velocity  $u_0$  is split into the components  $u_0$ ,  $x(z) = u_0(z) \cdot \sin(\theta_0)$  and  $u_0,y(z) = u_0(z) \cdot \cos(\theta_0)$ , where  $\theta_0$  is the yaw angle

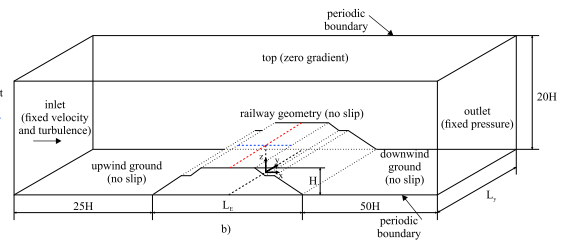


Fig. 2. Scheme of computational domain and boundary conditions (not in scale - superstructure not drawn for sake of clarity).

with respect to the railway longitudinal axis  $y$  (Fig. 2(a)). The combination of the railway arrangement in the domain and adopted b.c. at inlet and side surfaces allows to keep the same spatial grid for any yaw angle, and to avoid tip effects at the end of the embankment. Conversely, the first approach does not offer the mentioned advantages, as discussed in (Tomasini et al., 2014; Noguchi et al., 2019).

### 3.2. Numerical approach

The Finite Volume Method is adopted to numerically evaluate the flow-field. The space discretization is accomplished by a fully structured grid consisting of hexahedral cells. A slice of the grid in the vertical  $x - z$  plane is shown in the background of Fig. 3(a). This grid topology is extruded in the  $y$  direction by a constant step equal to  $\Delta_y = 0.026H$ . The resulting grid at the ground surface is shown in the same figure.

The following criteria have led the grid generation and, in particular, its refinement around the ground and the railway: i. the geometry of the rail web and head is precisely discretized (Fig. 3(b)) in order to accurately simulate the local flow around them. Bridging between different geometrical scales and related grid densities is a demanding goal, being the rail height up to about 1/74 the substructure height, i.e. about 1/6600 the along-wind size of the whole domain; ii. the overall cell number is limited and related computational cost affordable in the framework of a wide parametrical study; iii. the cell aspect ratio is kept lower or equal to 100, namely close to the ground and far from the railway; iv. the height  $n_w$  of the wall-adjacent cells provides a sufficiently high grid resolution in the normal direction  $n$  to the surface in order to adequately resolve the gradients of flow variables; v.  $n_w$  complies with the wall function requirement on dimensionless wall unit  $30 < n^+ = n_p u^*/\nu < 200$ , being  $n_p = n_w/2$  the cell center height. In order to satisfy criteria iv. and v., the wall unit is in the range  $100 = n^+ \leq 200$  for all the simulations. The overall cell number of the resulting grid depends on the overall height  $H$  of the railway and on the adopted railway system. For sake of conciseness, reference is made here to the grid shown in Fig. 3, composed by  $6.8e+6$  cells.

The cell-centre values of the variables are interpolated at face locations using the second-order Central Difference Scheme for the diffusive terms. The convection terms are discretized by means of the so-called Limited Linear scheme, a 2nd order accurate bounded Total Variational Diminishing (TVD) scheme resulting from the application of the Sweby limiter (Sweby, 1984) to the central differencing in order to enforce a monotonicity criterion. The SIMPLE algorithm is used for pressure-velocity coupling. The open source code OpenFoam® is used. On average, a CPU time from 72 to 96 h is required for each simulation on Intel(R) Core(TM) i7 CPU 860 @ 2.80 GHz with 18 cores employed.

## 4. Setup of the study

### 4.1. Geometry of railway systems

The adopted Railway Systems (RS) result from multiple combinations of types of substructure and superstructure. Their geometries are selected among the ones currently used in railway construction, and observed during site visits along desert railways, as in Sect. 2. All of the resulting cases are listed in Table 1.

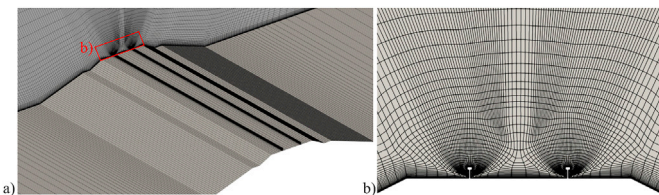


**Fig. 3.** Numerical grid around the ground and side surfaces of a standard railway (a), close up view around the rail (b).

The table is split into two parts: the first one (from cases EB.1 to EB.5) includes railway systems with standard sub and superstructure; the second one (from cases NC.1 to NC.4) collects railway systems with Non-Conventional superstructure. For the sake of clarity, each case is accompanied by a scheme of its geometry. For the sake of brevity, the values of geometric parameters constant among all the cases are given in Fig. 4. In particular, standard gauge equal to 1435 mm, and 172 mm high Vignole UIC 60 rails are adopted.

The main varying parameters are indicated by capital letters. Letter L stands for horizontal dimensions, H for vertical dimensions, and AR denotes a slope Aspect Ratio. Subscript E refers to embankment, B to ballast and r to rail.

Substructure is denoted by EB when it includes both Embankment and Ballast bed, while E stands for ballastless systems.  $AR_E$  and  $AR_B$  do not vary continuously because of earthworks construction constraints: most common discrete values are adopted and detailed in Table 1. Low ( $H_E = 1.2$  m) and high ( $H_E = 12$  m) embankments are tested as well. Additionally, case ID 0 is considered, where rails are laid directly on natural ground. This case is intentionally excluded from the list of railway systems because it does not follow railway construction practice, where a compacted subgrade of minimum thickness is always prescribed. Case 0 is conceived as an aerodynamic reference, i.e. as a geometrical and aerodynamic limit case where the substructure has no effects on the aerodynamics of the railway system.

Standard Superstructure (SS) includes rails supported by standard sleepers embedded in the ballast bed. Hence, sleepers do not affect the wind flow. Non-Conventional RS couple a single substructure geometry with four different kind of superstructures: i.) ballastless embankment with continuous beams (E-CB), analogous to the track system described by van der Merwe (2013) and shown in Fig. 1(h); ii.) ballastless embankment with slotted beams (E-SB) adopted as an intermediate step between (i. E-CB) and (iii. E-HS); iii.) embankment with ballast and humped sleepers (EB-HS), analogous to the track system described by Riessberger and Swanepoel (2005); Reissberger et al. (2016) and shown in Fig. 1(i); iv.) Ballastless embankment with humped slab (E-HS), analogous to the track system described by Zakeri (2012). The height of the beam in E-CB and E-SB is equal to 190 mm. The height of the humps in EB-HS and E-HS is equal to  $H_h = 140$  mm.

The total height of the railway system  $H$  includes humps or beams, if any. It is adopted as aerodynamic reference scale in the following.

### 4.2. Incoming wind flow and sand features

The incoming wind flow adopted in simulations reflects actual desert conditions. The ground aerodynamic roughness length is set equal to  $z_0 = 3e - 3$  m, according to the recommendations given in Eurocode1 (2005). The incoming far-field wind shear velocity is set equal to  $u_{*,0} = \sqrt{\tau_0/\rho} = 0.82$  m/s. Such a value is appropriately chosen in order to exceed the erosion threshold shear velocity  $u_{*,t}$  for sand grain diameters in the range  $d \in [0.063, 1.2]$  mm (Raffaele et al., 2016), i.e. windblown sand transport occurs upwind the railway. The resulting reference wind speed at the rail height varies in the range  $12.5 \leq U_H \leq 16.7$  m/s, and the corresponding Reynolds number  $Re_H = H \cdot U_H/\nu$  in  $1.88e+6 \leq Re_H \leq 2.12e+7$ . Such values, together with the railway sharp-edged geometry, suggests that the flow is within the Reynolds super-critical regime, so that significant Reynolds effects are not expected to take place for any of the cases. To take into account incoming wind not perpendicular to the alignment, simulations are carried out with yaw angle different than  $\theta_0 = 90^\circ$ .  $\theta_0 = 75^\circ, 60^\circ, 45^\circ$  are adopted for EB.1, NC.3 and NC.4 cases (Table 1).

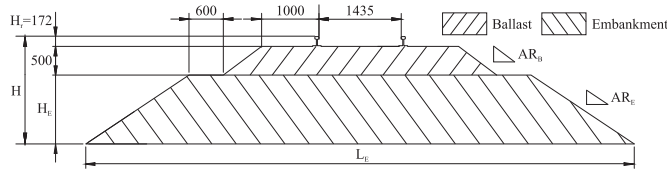
The adopted sand diameter  $d$  is equal to 0.2 mm, as the average value of diameters measured at the sites visited and presented in Fig. 2. The corresponding mean value of the erosion threshold shear stress is equal to  $\tau_t = 0.09$  Pa (Raffaele et al., 2016).

The windblown sand erosion/sedimentation is mainly triggered by

**Table 1**

Synopsis of conventional and non-conventional railway systems.

case ID	RS	$AR_E$	$H_E [m]$	$AR_B$	$\theta_0 [\text{deg}]$	geometrical scheme
0	–	–	–	–	90	
EB.1	EB – SS	3 : 1	1.2	2 : 1	90, 75, 60, 45	
EB.2	EB – SS	3 : 1	12	2 : 1	90	
EB.3	EB – SS	3 : 1	1.2	4 : 3	90	
EB.4	EB – SS	3 : 2	1.2	2 : 1	90	
EB.5	EB – SS	3 : 2	1.2	4 : 3	90	
NC.1	E – CB	3 : 1	1.2	–	90	
NC.2	E – SB	3 : 1	1.2	–	90	
NC.3	EB – HS	3 : 1	1.2	2 : 1	90, 75, 60, 45	
NC.4	E – HS	3 : 1	1.2	–	90, 75, 60, 45	

**Fig. 4.** Values of common geometrical parameters in mm, with reference to EB.1 cross section.

the local ratio of wind-induced local wall shear stress and sand threshold shear stress  $|\tau|/\tau_t$ . Fig. 5 graphs the  $\tau_0/\tau_t$  ratio for varying incoming wind velocity at 10 m height and sand diameter. The surface above the iso-contour  $\tau_0/\tau_t = 1$  corresponds to the  $U_{10} - d$  pairs that induce erosion.

In order to discuss potential erosion/sedimentation patterns in different environmental conditions, one can vary  $d$  and  $\tau_t$  in turn, or equivalently  $U_{10}$  and  $\tau_0$  in turn.  $d = 0.2$  mm is kept constant throughout the present study (thick black line in Fig. 5), while  $U_{10}$  is varied to sample four different classes in the Beaufort Scale (red points in Fig. 5): #1-BS 4 moderate breeze,  $\tau_0/\tau_t = 1.5$ ; #2-BS 5 fresh breeze,  $\tau_0/\tau_t = 3$ ; #3-BS 6 strong breeze,  $\tau_0/\tau_t = 6$ ; #4-BS 8 gale,  $\tau_0/\tau_t = 12$ .

Within a given aerodynamic regime, i.e. the supercritical one in this

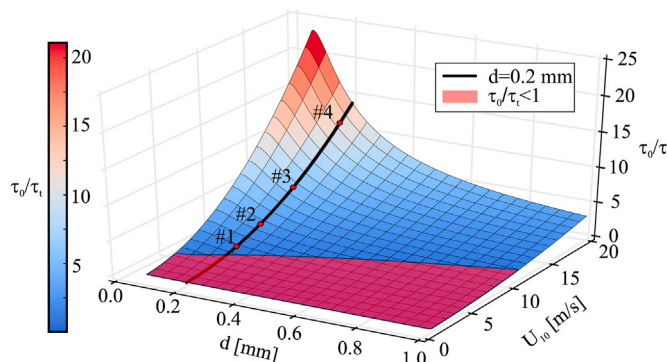
study, the wind-flow can be quantified by flow variables in dimensionless form thanks to aerodynamic similarity, as it is done in many engineering areas, e.g. by lift and drag coefficients. The dimensionless skin friction coefficient  $C_f = 2|\tau|/\rho U_{10}^2$  is obtained directly from simulations. Later, the local ratio  $|\tau|/\tau_t$  is obtained for each Beaufort scale by making  $C_f$  dimensional again with reference to the desired velocity:  $\tau_i(x, y, z) = C_f(x, y, z) \frac{1}{2} \rho U_{10,i}^2$ .

## 5. Results

Result analysis generally aims at discussing how different railway systems in a combination with different incoming winds modify the wind flow and the potential sand sedimentation/erosion conditions around the railway. For the sake of clarity, results are classified according to the scale to which different phenomena correspond to: i. global scale, and ii. local scale, the quantities of the latter being designated with subscript  $r$  (rail). Consistently, global and local spatial lengths are given in their dimensionless form with reference to the whole railway height  $H$  and the rail height  $H_r$ , respectively. Conversely, velocity is always normalized with reference to the velocity  $U_H$ . At the global scale, the flow is analyzed within the subdomain  $-7H \leq x \leq +16H$ : it includes the overall railway system and the downwind reversed flow region. At the local scale, the focus is put on the subdomain  $-11H_r \leq x \leq +11H_r$  which closely corresponds to the upper horizontal surface of the ballast bed or embankment. Subscripts  $R$  and  $S$  refer to recirculation and sedimentation zones, respectively. Subscripts  $u$ ,  $m$  and  $d$  designate upwind, mid-gauge, and downwind position along the  $x$ -direction. For instance,  $L_{R,d}$  is the length of local downwind recirculation.

### 5.1. Preliminary study

Specific and punctual benchmarking on railway embankment with track system and without rolling stock has not been carried out, because of the lack of publicly available, high-quality, fully described WT tests and related measurements of the local flow variables relevant to the present application. However, the whole computational model has been fully validated in Bruno and Fransos (2015) against accurate, local WT measurements for the same class of aerodynamic problems, i.e. the

**Fig. 5.** Ratio  $\tau_0/\tau_t$  at the inlet boundary as a function of  $d_s$  and  $U_{10}$ .

high-Re turbulent flow around a 3D bluff fundamental landform mounted on desert surface, characterized by boundary layer separation and reattachment. The adopted computational model, detailed in Section 3, is exactly the same in all its parts, that is turbulence model and boundary conditions, numerical approach, type of computational domain and spatial grid.

The preliminary study is intended to set the most suited track-wise length  $L_y$  under yawed incoming wind, in order to increase the computational efficiency. The preliminary study is carried out on EB.1 case under the widest amplitude of the yaw angle  $\theta_0 = 45^\circ$  regarded as the most challenging setup. Three values are tested in geometrical progression,  $L_y = 40H, 20H$ , and  $10H$ .

The x-wise distributions of the normalized x-component of the wall shear stress at  $y = 0$  are graphed Fig. 6(a) for every value of  $L_y$ . Two remarks follow: i. the adopted upwind  $L_{x,u}$  and downwind  $L_{x,d}$  windward lengths are long enough to guarantee no changes in the flow far upwind and downwind the railway, and proof is given that velocity and turbulence profiles at the inlet and the outlet are in equilibrium; ii. the three distributions overlap, i.e. no significant effects are induced by  $L_y$  in the considered range. The distance of the reattachment point downwind the track (recirculation length in the following) is equal to  $L_R = 6.78H$  at the central section. The  $L_R/H$  distribution along the y-direction in Fig. 6(b) testifies that the reattachment point position is constant trackwise, i.e. the flow is 2D, and that it is not affected once more by the  $L_y$  value. Slight and negligible oscillations only occur along the y-wise distribution of the normalized y-component of the wall shear stress sampled at  $x/H = 5$  (Fig. 6-c). From the presented, it can be concluded that the results obtained with the shortest crosswind length  $L_y = 10H$  do not significantly differ compared to the ones given by larger domains. Such a length is much smaller than the one adopted by Noguchi et al. (2019) ( $L_y = 25H$ ) thanks to the adopted combination of the computational domain and b.c. Although even shorter  $L_y$  values could be envisaged,  $L_y = 10H$  is adopted in the following, because of its acceptable computational cost.

## 5.2. Effects of substructure with conventional ballasted track

The main features of the flow field around the whole railway are exemplified in Fig. 7 for EB.1 case only for sake of brevity.

Fig. 7(a) shows the flow topology by means of streamlines coupled with vorticity field. The boundary layer shows high vorticity magnitude. Its large-scale separation involves the main clockwise vortex  $R_d$ . Such a recirculation area is bounded by two inflection points defined as those at which  $|\tau| = 0$ , namely the separation point at the downwind sharp edge of the ballast bed, and the downwind reattachment point. The outer free flow is quasi-irrotational. The profiles of the dimensionless velocity components ( $u_x/U_H$  and  $u_z/U_H$ ) are given in Fig. 7(p1)-(p7) along 4 selected vertical lines (p1, p2, p6, p7) around the substructure and 3 lines (p3, p4, p5) close to the track. Profiles are given for every EB.SS cases. p1 shows the upwards flow deflection induced by the substructure, that results in decreased  $u_x$  and  $\partial u_x/\partial z|_{z=0}$ , and potentially in sand sedimentation. Conversely, at p2 the flow is significantly accelerated in terms of both  $u_x/U_H$  and  $u_z/U_H$  and their z-derivative at the ground: erosion condition is qualitatively attended. The acceleration is most significantly affected by  $H$  at lower ( $z - z_g$ )/ $H$  (EB.2 case). The effects of  $AR_E$  and  $AR_B$

on  $u_z/U_H$  is greater than on  $u_x/U_H$ , p6 and p7 lay in undisturbed flow for case 0, while they are within the substructure wake for the EB.SS cases. p6 crosses the recirculation region, and the large negative z-derivative of  $u_x$  at the ground is expected to induce backwards erosion. p7 is located slightly downstream the reattachment of the boundary layer, and the weak z-derivative of  $u_x$  potentially promotes sedimentation. Along both lines, negative  $u_z/U_H$  is weakly affected by the substructure geometry, and reflects the downwards flow induced by recirculation. At p3-5, velocity components and their z-derivatives close to the ground are weakly affected by the substructure geometry, i.e. the local flow is mostly driven by the rails. Even for the case 0, the velocity profiles are close to the others. Conversely, at elevations approximately higher than the rail ( $(z - z_g)/H > 1$ )  $u_x/U_H$  is sensitive to the substructure geometry. In particular, for case EB.2 at p5 the rail-induced effects on the x-velocity profile almost vanish and embankment induced separation prevails.

In order to check and discuss the condition for sand erosion/sedimentation, Fig. 8 focuses on the shear stress field along ground and substructure surface. As in Fig. 7, only EB.1 case is shown for the sake of conciseness. The flow topology is included in sub Fig. 8(a) for reference. Global flow features are observed around the whole railway at the substructure scale.

The distribution of the skin friction coefficient  $C_f$  is plotted in Fig. 8(b). It is further rescaled in the dimensionless ratio  $\tau^* = \frac{\tau_x}{|\tau_x|} \frac{|t|}{\tau_t}$  in Fig. 8(c) to account for the effect of four incoming reference speeds  $U_{10}$  on the potential sand erosion/sedimentation conditions without the need of supplementary computational simulations. In the perspective of the study, the key values are  $\tau^* = \pm 1$  (erosion thresholds). The corresponding points at the sand surface where transition between sedimentation and erosion occurs are called sedimentation points. Three ranges directly result for  $\tau^*$  in Fig. 8(c), and corresponding patterns follow along the sand surface (Fig. 8-d): windward erosion (from now on simply called erosion,  $\tau^* > 1$ ), sedimentation ( $1 > \tau^* > -1$ ) and backward erosion ( $\tau^* < -1$ ). Recirculation area with local reversed flow close to the sand surface is a necessary condition for backward erosion. Considerably different sedimentation patterns take place in the downwind recirculation zone, and upwind the substructure to a lesser extent. In general, as  $U_{10}$  increases, both erosion and/or backward erosion zones replace the sedimentation, i.e. sedimentation areas shorten and erosion ones grow. In particular, downwind faces of embankment and ballast lay in the downwind recirculation zone. For the lowest value of  $U_{10}$  (#1) such faces are entirely in the sedimentation zone. As  $U_{10}$  increases (#2, #3), localized short backward erosion zones take place. For the highest  $U_{10}$  (#4), such zones coalesce, and the downwind face is entirely backward eroded. Upwind slopes of embankment and ballast lay in the erosion zone for all cases, because of the local flow acceleration. Upwind embankment and ballast feet are the exceptions because of the local flow deceleration and the small local recirculation zone, respectively. As  $U_{10}$  progressively increases, sedimentation zones shorten upwind the embankment foot, while backward erosion takes place along the horizontal surface between embankment and ballast.

In order to synthetically quantify the effects of the incoming flow on global sedimentation/erosion/backward erosion, two lengths are defined in Fig. 8(d): the upwind sedimentation/backwards erosion length  $L_{S,u}$  measured from the first sedimentation point to the upwind foot of the

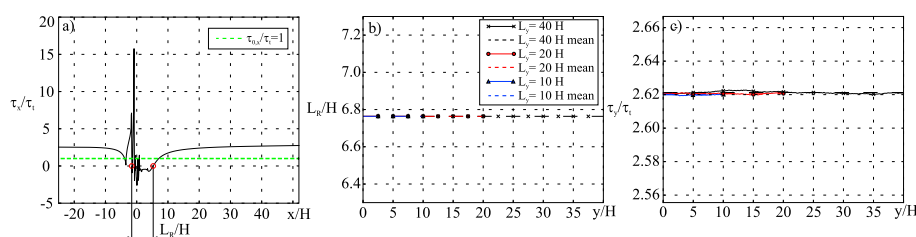
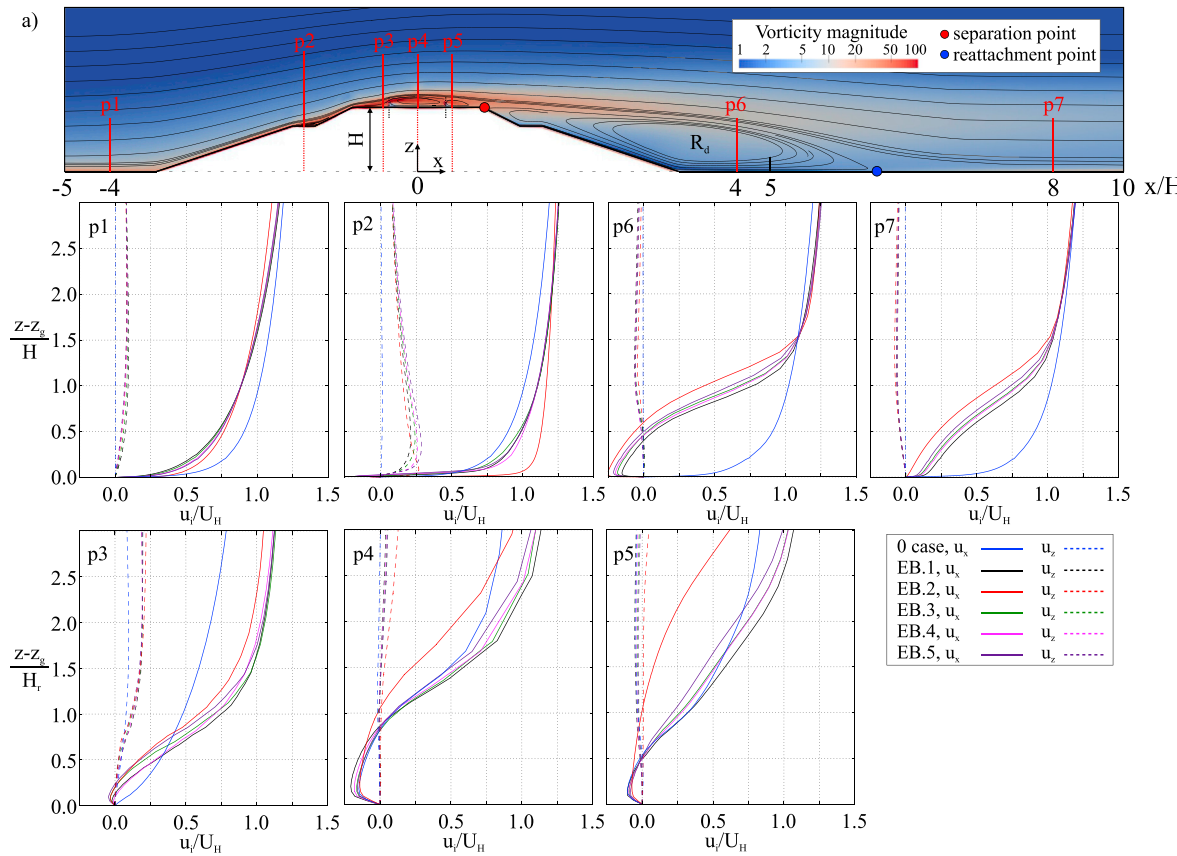
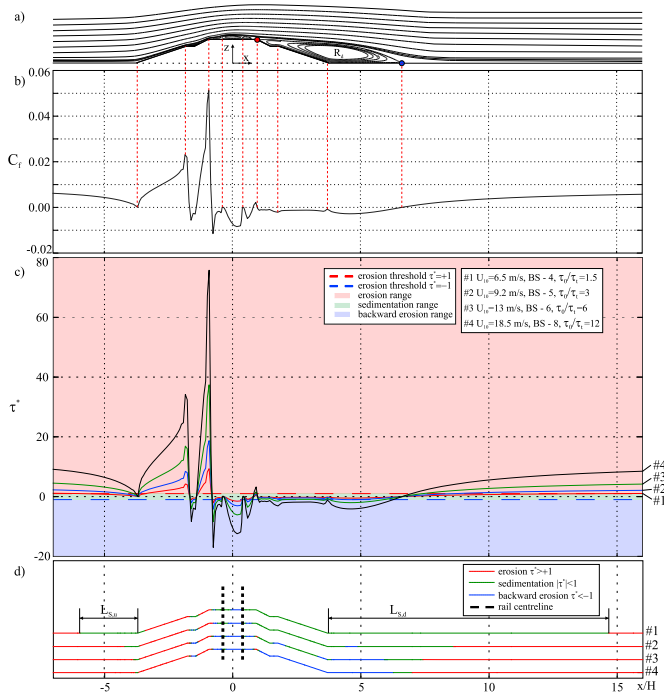


Fig. 6. Grid sensitivity to domain track-wise length  $L_y$ .



**Fig. 7.** Wind flow around railway: a) Streamlines and vorticity; p1-p7) Vertical profiles of the velocity components at different positions across the railway system.



**Fig. 8.** Global flow features and potential sedimentation zones: a) reference flow topology; b) Skin friction coefficient; c) Shear stresses for different incoming reference velocities; d) Potential sedimentation, erosion and backward erosion zones.

embankment; and the downwind sedimentation/backwards erosion length  $L_{S,d}$  measured from the downwind foot of the embankment to the last sedimentation point. It is worth stressing that both lines are defined between a fixed geometric point and a flow-dependent sedimentation point. Such lengths are plotted in Fig. 9 versus  $\tau_0/\tau_t$  with a much denser sampling. Additionally, case EB.1 is compared with other cases of standard railway geometry in order to point out the effects of different substructure geometry.

Both  $L_{S,u}/H$  and  $L_{S,d}/H$  monotonically decrease as  $\tau_0/\tau_t$  increases for all the cases, and tend to asymptotic values for  $\tau_0/\tau_t \rightarrow \infty$ . The horizontal asymptotes are equal to 0 for  $L_{S,u}/H$  in cases EB.1, EB.2 and EB.3, while  $L_{S,u}/H$  in the other cases and  $L_{S,d}/H$  tend to asymptotic values different than 0. In order to explain this, it is preliminary worth stressing that the position of the inflection points does not change in the rescaled graphs of  $\tau^*$ , while the position of the sedimentation points depends on the incoming wind speed  $U_{10}$  (Fig. 8-d). Hence, as  $\tau_0/\tau_t$  increases,  $\tau^*$  curve is steeper, so that the  $x$ -distance between the inflection point and its neighboring sedimentation points decreases. At the limit case  $\tau_0/\tau_t \rightarrow \infty$ , such a distance tends to 0. It follows that in case of recirculation the sedimentation points collide into the inflection point, and  $L_S$  tends to the distance between the fixed geometrical point and the inflection point. In case of deceleration, inflection point does not occur, sedimentation points collide into the fixed geometrical point and  $L_S \rightarrow 0$ . In the light of this, graphs in Fig. 9(a) prove that upwind recirculation occurs in front of the embankment for cases EB.4 and EB.5, while it does not for cases EB.1, EB.2 and EB.3. In other terms, embankments with aspect ratio  $AR_E = 3 : 2$  leads to a reversed flow at their foot, while gentler  $AR_E = 3 : 1$  simply involves flow deceleration. Additionally, the embankment height  $H_E$  and the ballast slope  $AR_B$  have no significant influence on the upwind sedimentation length, as testified by the grouping of the curves with equal  $AR_E$ . Conversely, all curves of  $L_{S,d}$  (Fig. 9-b) are clearly distinct, although they share the same trend. It follows that all the substructure parameters

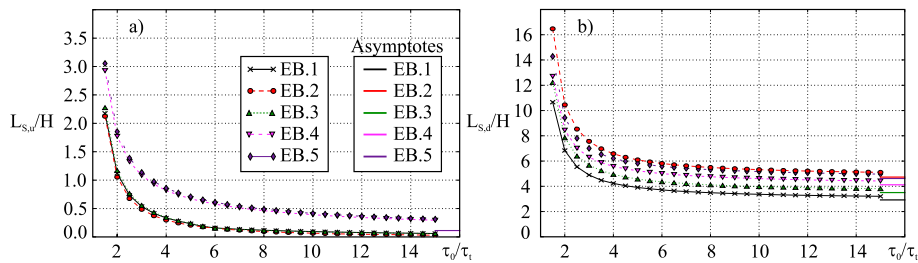


Fig. 9. Global upwind (a) and downwind (b) sedimentation lengths.

affect the sedimentation downwind the embankment. The steeper the embankment ( $AR_E$ , e.g. compare EB.1 and EB.4) and the ballast bed ( $AR_B$ , e.g. compare EB.1 and EB.3), the longer  $L_{S,d}/H$ . In spite of this common trend, the effect of a steeper embankment is twice the one of a steeper ballast, in average over the whole range of  $\tau_0/\tau_i$ .

The influence of  $H_E$  is evaluated by comparing EB.1 and EB.2 cases. An increase of 10 times the height of the embankment results in an increase of 1.5 time of  $L_{S,d}/H$ . An analogous effect is obtained by increasing at the same time both  $AR_E$  and  $AR_B$  (compare EB.2 and EB.5) for every value of  $\tau_0/\tau_i$ .

Local flow features are observed along the track at the rail scale. In Fig. 10 all the EB-SS cases, together with case 0, are shown analogously to Figs. 7 (a) and 8 (d). Vorticity coupled with streamlines are shown in the left column, while the right column shows the sedimentation, erosion and backward erosion zones. Each row of the figure corresponds to a

single EB-SS case. The different flow conditions shown in the right column are in order #1, #2, #3 and #4, from top to the bottom.

Three significant local flow coherent structures develop: i.) upwind local vortex  $R_{u,r}$ , positioned upwind the upwind rail; ii.) middle local vortex  $R_{m,r}$ , spanning along the gauge; iii.) downwind local vortex  $R_{d,r}$ , located downwind the downwind rail. Additional secondary vortices appear in some cases upwind and downwind the rails. From the cases 0, EB.1 and EB.2 it can be seen that the height of the substructure affects the shape of the mid-rail vortex  $R_{m,r}$  and the position of its center. For the lowest  $H = 0$  (case 0), it is downwind the upwind rail, for  $H = 1.7$  m (case EB.1) it moves at about the middle of the gauge, while for the highest  $H = 12.5$  m (case EB.2), it shifts towards the downwind rail. The lower the substructure, the flatter all the vortices, and the shorter the x-length of the downwind one  $R_{d,r}$ . Significant difference arises in the topology of  $R_{d,r}$  in EB.2, where it coalesces with the downwind global vortex  $R_d$ . All

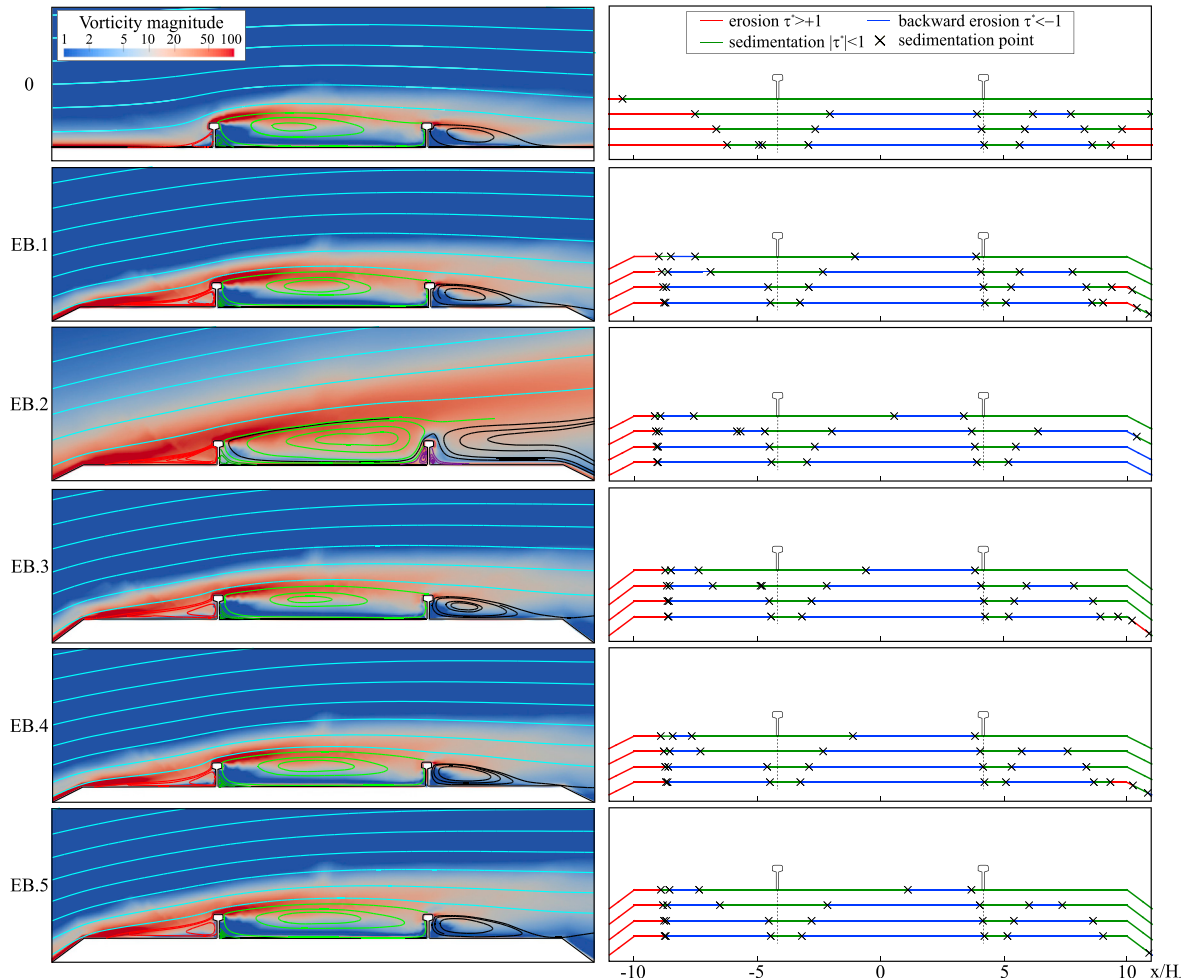


Fig. 10. Local flow patterns (left column) and potential sedimentation, erosion and backward erosion zones (right column).

the features above are due to significantly different direction of the flow just outside the boundary layer at its separation point in correspondence with the upwind rail. In particular, local upward flow does not allow the flow to reattach at the downwind surface of the ballast. No significant differences in the flow structure occur for the rest of the cases (EB.3, EB.4, EB.5) compared to EB.1 case, i.e.  $AR_E$  and  $AR_B$  do not qualitatively affect the local topology of the flow.

Right column of Fig. 10 testifies that for each recirculation zone, many sedimentation and backward erosion zones occur, and they significantly depend on the incoming flow speed. Three general rules can be outlined for their reading: i. the ballast upwind sharp edge is constantly eroded, because of the flow speedup; ii. along recirculation zones, sedimentation and backward erosion take turns, depending on the streamline curvature close to the wall and to the incoming speed; iii. the eventual reattachment point along the ballast downwind surface (e.g. in 0, EB.1, EB.3, EB.4, EB.5) results in the sequence of backward erosion-sedimentation-erosion, being the latter strongly dependent on the extent of the reattachment and incoming speed (e.g. in 0, EB.1, EB.4). Due to alternating and varying sedimentation and erosion zones, corresponding bulk areas ( $A_S$  and  $A_E$ ) are defined instead of single sedimentation or erosion length. The areas are expressed as the integrals of sedimentation and erosion zones, respectively, along the whole ballast horizontal surface  $A_u$  ( $-10 = x/H_r \leq 10$ ), and are further divided by  $A_u$  itself. The resulting dimensionless bulk quantities  $A_S/A_u$  and  $A_E/A_u$  can vary in the range [0, 1]. The backward erosion area straightforwardly follows from the previous ones as  $A_{BE} = A_u - (A_S + A_E)$ .  $A_S/A_u$  and  $A_E/A_u$  are plotted versus  $\tau_0/\tau_t$  in Fig. 11 (a) and (b), respectively.

Case 0 behaves significantly different than other cases. Sedimentation occurs everywhere for the lowest  $\tau_0/\tau_t = 1.5$ , while both  $A_S/A_u$  and  $A_E/A_u$  are higher than in the other EB-SS cases for higher  $\tau_0/\tau_t$ . This behaviour mainly results from the lack of backward erosion upwind the upwind rail for every  $\tau_0/\tau_t$  (Fig. 10). The other EB-SS cases slightly differ for low-to-moderate values  $\tau_0/\tau_t \leq 6$ , where the rate of change of  $A_S/A_u$  depends in general on the local switch from sedimentation to erosion. For higher values  $\tau_0/\tau_t > 6$  the local sedimentation/erosion pattern along the track is nearly constant and does not dramatically depend on the substructure geometry.

### 5.3. Effects of non-conventional track systems

The aerodynamic and sedimentation behaviour of the Non-Conventional Railway Systems listed in Table 1 under orthogonal wind is discussed in this Section. All cases share the same substructure adopted in EB.1.

Except for NC.1, all cases considered have periodic trackwise varying geometry, because of the humped sleepers/slab and gaps among them. The spacing between them is the same in all cases and equal to  $W = 0.6$  m. From the aerodynamic point of view, the humps make the whole railway as a bluff-body with small periodic perturbations, and a 3D local flow is expected. Analogous setups have been studied in literature during the last decade, and adopted to control the flow around bluff cylinders under uniform incoming flow. Interested readers can refer to the review papers by Choi et al. (2008) and Demartino and Ricciardelli (2017) and references therein. For such a class of flow, periodic structures in the

wake result from perturbations. In particular, Kim and Choi (2019) recently showed that the largest flow structures in the wake can have a spanwise length scale  $\lambda$  not necessarily equal to the wavelength of the periodic perturbations ( $\lambda \geq W$  for the present application).

In order to check the possible periodicity in the wake of the humps and to evaluate its trackwise length scale,  $u_y/U_H$  velocity component is plotted versus  $y/W$  along a sampling line in Fig. 12.

The  $y$ -wise sampling line is located half of the hump length downwind the upwind hump, and at a height from the ballast bed equal to half of the hump. Three emerging flow features can be easily recognized. They clearly and significantly depend on the hump shape and on presence or not of the ballast bed. First, the track-wise length scale significantly varies, being  $\lambda_2 = 3W$ ,  $\lambda_3 = 4W$  and  $\lambda_4 = W$  for NC.2, NC.3 and NC.4 respectively. Second, the maximum magnitude of  $u_y/U_H$  differs among cases as well, being the highest for NC.2., while NC.3 and NC.4 share approximately the same value. Third, the same trackwise periodic trend is qualitatively different. The flow around the ballastless humped slab (NC.4) is almost perfectly periodic, and the local flow almost symmetric with respect to the mean vertical plane of each gap, i.e.  $u_y = 0$ . The flow around the rounded humped sleepers (NC.3) is not periodic, it seems characterized by multiple length scales, and adjacent gaps by recurrent sequence of positive-nil-negative-nil  $u_y$  vectors. The flow around sharp-edged slotted beams (NC.2) is nearly periodic, but  $u_y$  distribution along  $\lambda$  is asymmetric and featured by a recurrent sequence of positive-weakly positive-weakly negative-nil  $u_y$  vectors.

In order to shed some more light on the 3D features of the local flow, the patterns are visualized along a  $2W$ -long segment, named ‘streamline visualization field’ (s.v.f) in Fig. 12, and done in Fig. 13.

For sake of readability, domain equal to whole  $\lambda$  is omitted for NC.2 and NC.3. The flow around EB.1 case is included for aerodynamic reference, together with the 2D flow around NC.1 case. Left column corresponds to the domain around the upwind rail, while the right column to the downwind rail. The flow direction at solid walls is visualized by means of the Line Integral Convolution (LIC, Cabral and Leedom, 1993) applied to the  $\tau$  field. Each visualization field is further split in the middle along the  $y$  axis. The right half is dedicated to streamlines, while the left side to selected separation, reattachment and stagnation lines and point obtained from the  $\tau$  field. To keep the cases in the figure comparable, streamlines are seeded always in the same relative position and with the same seeding density for the more complex cases (NC.2–4).

The flow structures do not develop in the  $y$ -direction for NC.1, resulting in a 2D flow. Recirculation zones are larger than in EB.1 because of the higher blockage effect of the continuous beams. Upwind and downwind recirculation zones are qualitatively the same as in EB.1 case, except for additional smaller recirculation zones along the top flat surfaces of the continuous beams. Conversely, between the rails the flow is split into a large clockwise recirculation and a significant secondary counter-clockwise recirculation. The bounds of the recirculation zones correspond to separation, reattachment and stagnation straight lines. The stepped geometry of continuous beams and top rails involve the doubling of local recirculation, and corresponding stagnation and reattachment lines at both upwind and downwind side.

The upwind flow structure among cases NC.2–NC.4 is overall the same (Fig. 13, left column). The straight separation lines testify the flow is 2D

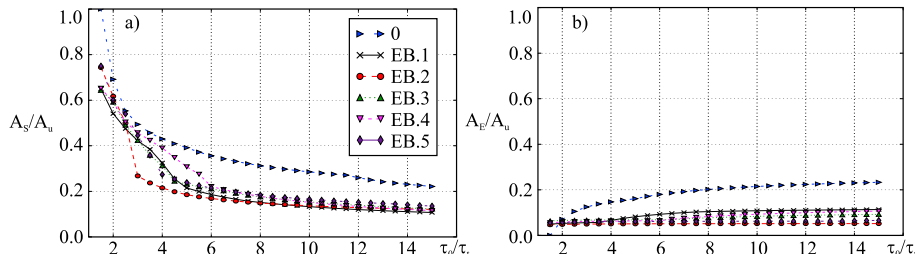
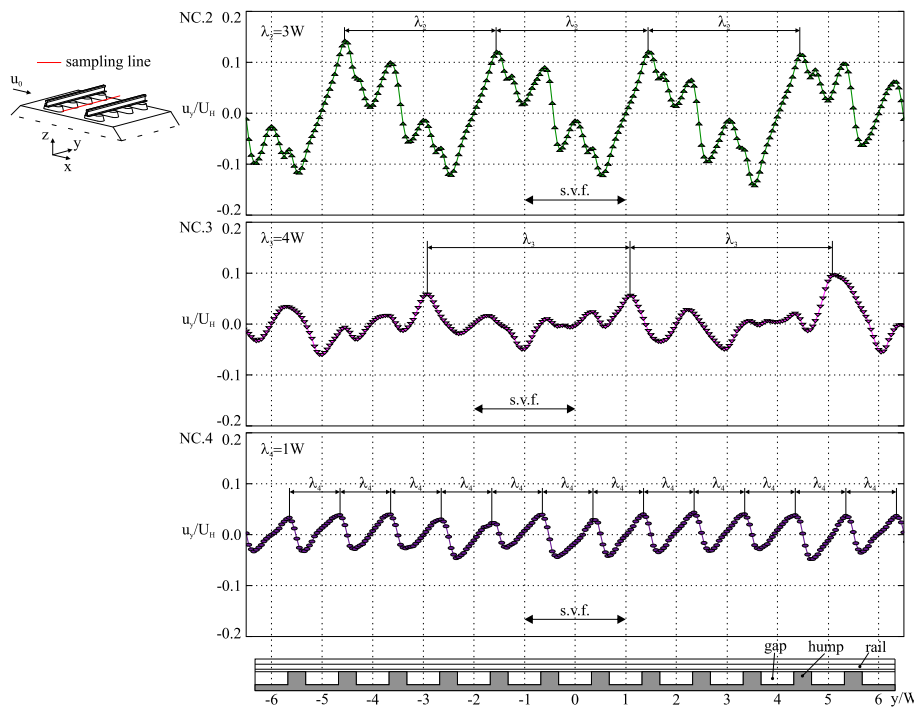


Fig. 11. Local erosion (a) and sedimentation (b) normalized areas for EB-SS cases.



**Fig. 12.**  $u_y$  velocity component along the trackwise direction for non conventional 3D superstructures (NC.2-NC.4).

far upwind the railway system. Conversely, the reattachment line around the upwind humps is not straight and is qualitatively different for humps with sharp or smoothed edges. For all the cases, stagnation occurs on both the upwind hump and rail surface, analogously to NC.1. Instead of a line, the stagnation is pointwise because of the 3D flow. The stagnation point on the upwind hump face is nearly at the same height for all cases. Conversely, the stagnation point on the rail web corresponds to the mid plane of the gap. The higher the momentum of the accelerated flow along the gap, the lower its position. On top of the humps a pair of counter rotating vortices with vertical axis of rotation occur. Because of their effect, the separation line along the rail head is no longer straight.

In spite of its very complicate topology, the flow along the gauge and around the downwind humps (Fig. 13, right column) can be overall explained by a single reading key, i.e. the interaction between the impinging jet flow induced by the upwind gap and the reversed flow along the downwind ballast surface induced by the global recirculation downwind the substructure. In cases NC.2 and NC.4 the jet flow prevails, while in NC.3 the reversed flow supersedes. The consequences are manifold. First, the flow along the downwind gap is windward in NC.2 and NC.4, while it is reversed in NC.3 (red arrows in Fig. 13). Second, the local flow results in the different position of stagnation points on the rail web: it corresponds to the one on the hump in NC.2 and NC.4, while it is located at the mid-plane of the gap in NC.3. Third, separation lines along the gauge are nearly directed x-wise and develop from one hump to the other in NC.2 and NC.4. Conversely, in NC.3 separation line along the gauge is deviated along the y axis and moved upwind by the reversed flow entering the downwind gap.

The 3D flow fields described above deeply impact the sedimentation, erosion and backward erosion patterns around the railway track surface. They are shown in Fig. 14 by plan views. The upper surface of continuous beams (NC.1) and humps (NC.2-NC.4) are excluded for sake of clarity.

The large secondary recirculation along the gauge in NC.1 leads to a corresponding sedimentation zone wider than in EB.1 for every incoming wind speed. The intricate 3D flow described in NC.2-NC.4 leads to sand sedimentation patterns varying both track-wise and alongwind in turn. The patterns periodically repeat track-wise with the same wavelength  $\lambda_i$ . The windward flow through both upwind and downwind gaps in NC.2 and NC.4 results in erosion patches under the downwind rail too. Such

erosion zones already occur in NC.2 for the lowest considered wind speed (#1), and progressively enlarge as wind speed increases. From #3, upwind and downwind erosion zones coalesce, and an along-wind “sand erosion channel” takes place for two gaps every three ones. Conversely, in NC.4 erosion along the downwind gap takes over sedimentation for high speed only (#3-#4), and never merges with erosion at upwind gap. The reversed flow across the downwind gap in NC.3 induces extensive sedimentation along the gauge and around the downwind humps (#1), progressively replaced by backward erosion zones as wind speed increases (#2-#4). Although these patterns map necessary conditions for sedimentation and erosion only, they allow to conjecture expected windblown sand dynamics. A sand erosion channel as in NC.2 is the most promising scenario, because it permits the free passage of sand through superstructure. Conversely, erosion at the upwind gap and backward erosion at the downwind one as in NC.3 is expected to move the sand from the downwind rail towards the middle of the gauge, i.e. to trap sand at the track. Such a scenario qualitatively echoes and explain the field evidence shown in Fig. 1(i), and partially defeats the purpose of ballasted humped sleepers.

All cases discussed above are synthetically compared by means of the dimensionless bulk quantities  $A_S/A_u$  and  $A_E/A_u$  in Fig. 15.

Even though NC.3 case has the lowest sedimentation area for  $\tau_0/\tau_t > 4$ , most of the erosion occurs backward. Conversely, NC.2 shows relatively low sedimentation and the highest erosion in the whole range of  $\tau_0/\tau_t$ . NC.4 case shows high erosion, but also very high sedimentation. The worst scenario is observed in NC.1, that combines the highest sedimentation with the lowest erosion. Standard railway system has intermediate performances in terms of sedimentation, but it is affected by very low erosion. In the light of this, the best performances under orthogonal incoming wind are observed for NC.2 and NC.4.

#### 5.4. Effects of yaw angle

In the light of the above, the effects of the yaw angle  $\theta_0$  of the incoming wind are evaluated for a selected number of cases: a conventional track system (EB.1), and two non-conventional ones (NC.3 and NC.4). For sake of conciseness, the global aerodynamics is scrutinized for EB.1 only in Fig. 16.

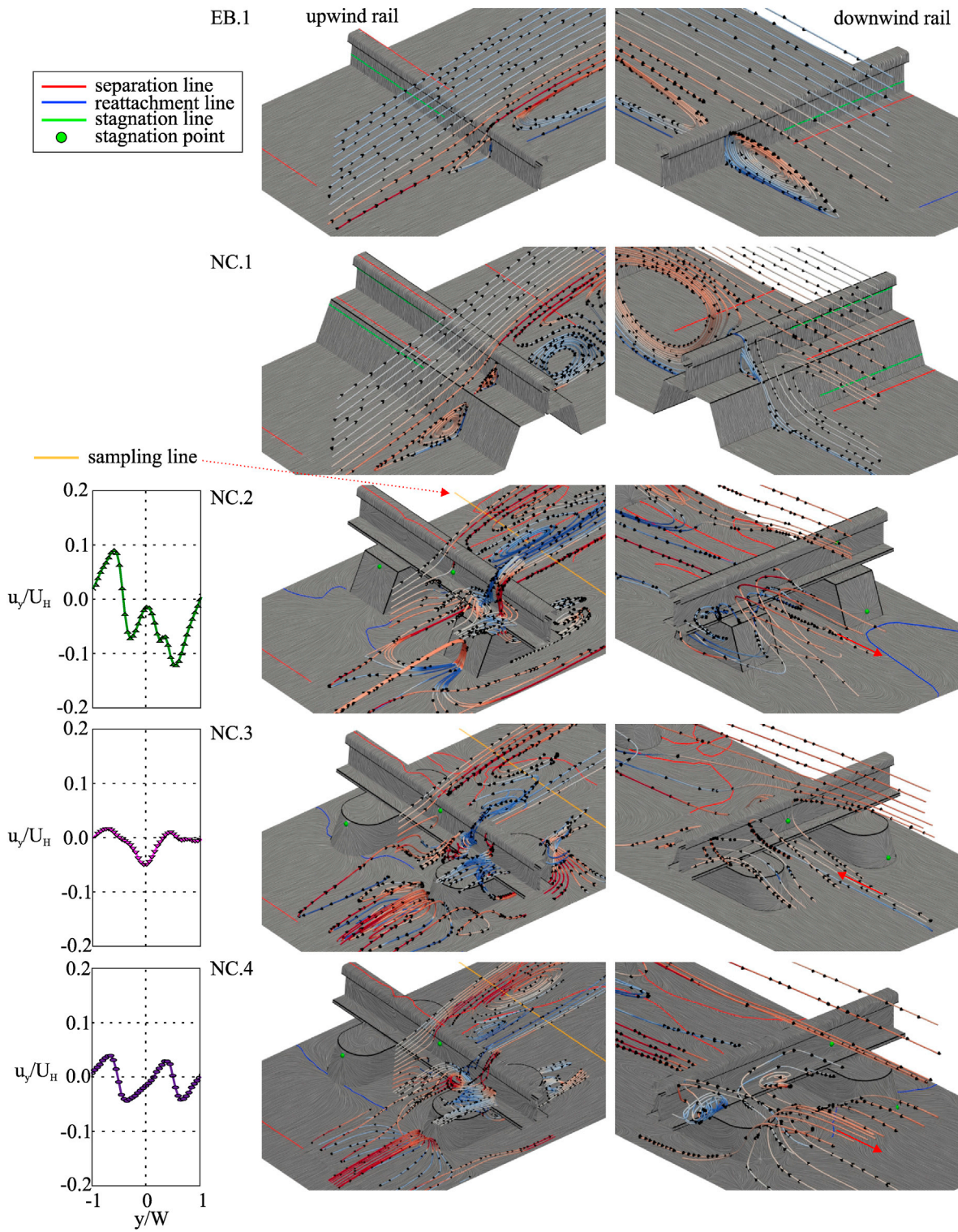
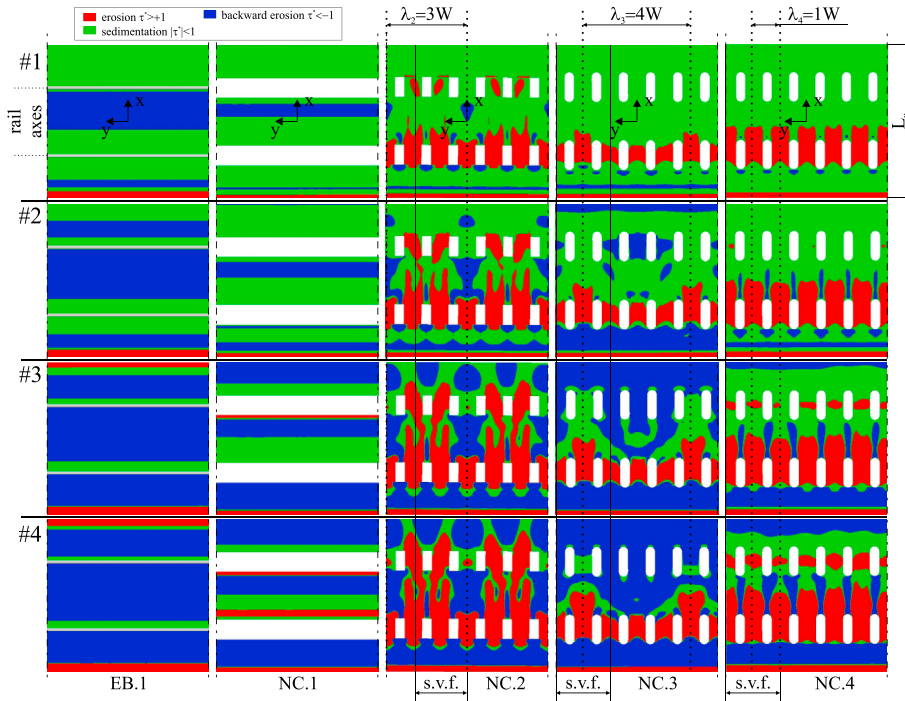


Fig. 13. Flow patterns for NC cases (incoming wind from left to right).

The global flow field is visualized by streamlines in plan view for the most yawed wind ( $\theta_0 = 45^\circ$ ) in Fig. 16(a). Blue streamlines are seeded in the outer free flow just outside the boundary layer, while red and green ones develop in the recirculation regions downstream the superstructure and between the rails, respectively. The outer flow is clearly deflected downwind the railway, being the angle shift  $\Delta\theta \approx 20^\circ$ . Such a feature echoes the known flow deflection downwind transverse desert and coastal dunes, discussed in Bauer et al. (2013) and references therein.

Red and green streamlines confirm boundary layer globally and locally separates, and testify the resulting recirculating flow is highly swirled. Also such feature recalls the so-called ‘helical’ or ‘corkscrew’ vortex in the near wake of transverse desert and coastal dunes, as discussed, measured and simulated e.g. by Walker and Nickling (2002), Delgado-Fernandez et al. (2013) and Jackson et al. (2013), respectively. Deflected outer flow and swirled recirculating flow coexist, unlike suggested by the seminal conceptual model proposed by Sweet and Kocurek (1990) for the



**Fig. 14.** Potential sedimentation, erosion and backward erosion patterns for NC cases (incoming wind from below).

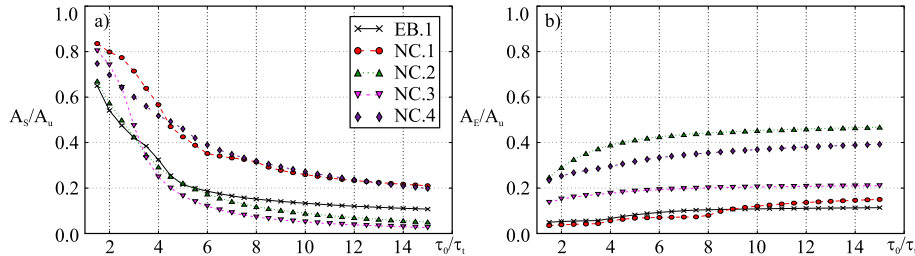


**Fig. 15.** Local erosion (a) and sedimentation (b) normalized areas for NC cases.

lee-side flow of aeolian dunes.

In the spirit of the study, the effects of the yaw angle are further scrutinized by referring to the  $x$  and  $y$  components of the shear stress at ground.  $\tau_x$  and  $\tau_y$  components are normalized by the corresponding component at the inlet, and plotted versus the  $x$  axis in Fig. 16(b) and (c), respectively. Gray stripes hide the highly localized effects induced by sharp edges and rails in narrow ranges ( $\pm H_r$ ), where the results are unreadable at the adopted scale because of very high gradients of  $\tau$ . Two significant behaviors are observed. First, the normalization leads to all the curves nearly overlapping. The results prove that Prandtl's independence principle Schlichting (1979) also holds for turbulent flow around rail embankments (Baker, 1985; Noguchi et al., 2019) far from local perturbations. Second, the change in magnitude of  $\tau_y/\tau_{0,x}$  is approximately twice the change of  $\tau_y/\tau_{0,y}$ . Moreover,  $\tau_y$  never changes sign, i.e.  $\tau_x$  is the sole cause of the switch between potential erosion and backward erosion, if any. The local angle between the alignment direction and the resultant  $\tau$  vector follows from its components  $\theta = \text{atan}(\tau_y/\tau_x)$ . The distribution of  $\theta/\theta_0$  is graphed in Fig. 16(d). Under incoming orthogonal wind,  $\theta$  takes only two values, i.e.  $\theta = \pm 90^\circ$ , where  $\theta = -90^\circ$  correspond to reversed flow. Conversely, continuous distributions occur under yawed winds, due to the fact that  $\tau$  components vary differently. Such distributions prove that the boundary layer flow is locally deflected, and that the local switch in direction depends on the yaw angle. In particular, all distributions reach  $\theta/\theta_0 = 0^\circ$  at the upwind foot of the embankment, because of the  $x$ -wise deceleration. In more explicit terms, at the upwind

foot the local flow perfectly aligns with the railway. The flow deflection at the embankment upwind foot is qualitatively analogous to the one observed in field trials along beach-dune and discussed by Bauer et al. (2012), Hesp et al. (2015) and cited references therein. The local boundary layer flow direction  $\theta$  is explicitly given in Fig. 16(e) by arrows and amplitudes at selected positions p1-p7. p1 and p7 are located far upwind and downwind respectively, p4 in the middle of the railway system, p3 and p5 in the middle of the upwind and downwind slope of the embankment, and p2 and p6 at the upwind and downwind embankment foot respectively. In the same Figure, potential erosion, sedimentation, and backward erosion patterns under 4 yaw angles and 4 reference speeds (#1 - #4) are also given. Two main remarks follow. First, for a given wind speed, the more yawed the incoming wind, the smaller the sedimentation zones. In other terms, skewed winds induce wider erosion and/or backward erosion under the same speed. In a supplementary reading, yawed incoming winds anticipate the switch from sedimentation to erosion at a given location. For instance, at the embankment upwind foot (p2) sedimentation holds at every speed when  $\theta = 90^\circ$ , but trackwise erosion takes place starting with strong breeze (#3) for  $\theta = 60^\circ$ , and with fresh breeze (#2) for  $\theta = 45^\circ$ . The trackwise sand flow made possible by such erosion conditions is recognized along the toe of coastal dunes by e.g. Walker et al. (2006) and termed 'along-shore transport'. Analogously, along the embankment downwind slope (p5) backward erosion takes place uniquely under gale wind (#4) for  $\theta = 90^\circ$ , but it early occurs nearly trackwise ( $\theta = -14^\circ$ ) starting with

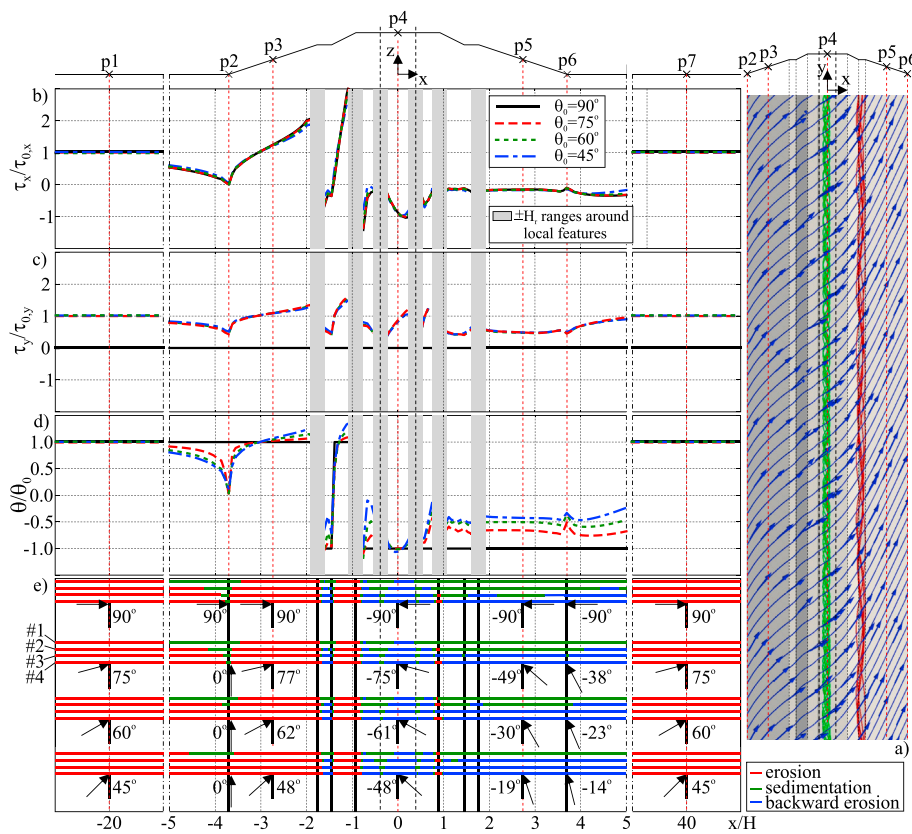


**Fig. 16.** Effects of differently yawed wind-flow on standard railway system (EB.1) aerodynamics.

fresh breeze (#2) for  $\theta = 45^\circ$ . In spite of significant differences in substructure geometry and track system, the case  $\theta_0 = 45^\circ$  qualitatively echoes to the field evidence shown in Fig. 1 (j), where ripples suggest the local wind blows at around  $\theta \approx 45^\circ$  upwind the railway, and at much lower negative  $\theta \approx -20^\circ$  downwind.

The effects of yawed wind-flow on the non-conventional superstructure are presented for cases NC.3 and NC.4. In Fig. 17 potential sedimentation, erosion and backward erosion patterns are shown for different  $\theta_0$ .

The simulated patterns are overall complicate, and locally highly sensitive to both the yaw angle and the track system. Nevertheless, some general features can be synthetically outlined. First, the patterns remain periodic track-wise also under yawed winds but, unlike orthogonal wind, the  $y$ -wavelength  $\lambda$  equals the spacing between humps  $W$ . Second, the shape of the sedimentation patches around downwind humps for high speed (#2 to 4) suggests the local flow direction in their wake. Here, the flow is reversed for NC.3 whichever the yaw angle. Conversely, for NC.4 the local flow is windward at  $\theta_0 = 75^\circ$  and  $\theta_0 = 45^\circ$ , while it is revealed to be reversed for  $\theta_0 = 60^\circ$ . Third, as wind speed increases, sedimentation is generally replaced by backward erosion, while erosion remains nearly constant or slightly decreases (NC.4,  $\theta_0 = 75^\circ$ , upwind gaps). The pattern for case NC.3- $\theta_0 = 75^\circ$ -#4 remarkably recall the field evidence observed for the same track system and shown in Fig. 1 (i): both gaps are eroded, and the combination of the sediment transport from the upwind and downwind gaps results in almost  $x$ -symmetric,  $y$ -periodic piles of sand within the gauge.

All the discussed cases are synthetically compared by means of dimensionless sedimentation and erosion areas in Fig. 18. The #1–4 curves are given for each case versus  $\theta_0$ .

In general, the cases show the highest sedimentation levels under perpendicular winds, that are proven to be the most critical with respect to sand covering. As the angle increases, sedimentation unexpectedly drops. Changes in incoming wind velocity have little influence on the

trend of the curves, while they generally translate/scale the curves w.r.t. the vertical axis. In particular, sedimentation and erosion on standard railway system (EB.1) are weakly sensitive to  $\theta_0$ : erosion slightly increases for more yawed winds, and sedimentation progressively decreases. NC.3 is nearly insensitive to  $\theta_0$ , except for its sedimentation at #1 speed, where  $A_s/A_u$  singularly increases as the yaw angle decreases. The case NC.4 is the most sensitive to changes in yaw angle in both erosion and sedimentation. Interestingly, their trend is not linear, and local minima occur at  $\theta_0 = 60^\circ$  because of the reversed flow around the downwind humps, as discussed in Fig. 17.

## 6. Conclusion

This paper contributes to increase knowledge about the flow around railway tracks, and the resulting potential sand sedimentation patterns. The study critically compares the aerodynamic behavior and related potential sand sedimentation/erosion patterns for different combinations of railway substructures and track systems which are usually adopted, namely in arid environments. The reading of the simulated flow field allows to point out the geometrical features of the railway substructure and superstructure with the most significant impact, and to understand the aerodynamic phenomena that induce necessary conditions for sand erosion and sedimentation. The potential sand sedimentation/erosion patterns depend not only on the flow dimensionless metrics usually employed in aerodynamics, but also on the ratio between the local shear stress and the sand erosion threshold value. Bulk dimensionless metrics of the sedimentation, erosion, and backward erosion allow to synthetically and generally define the performances for different railway systems.

In a synthetic design perspective, the most relevant results are outlined:

- low-rise, gentle-sloped substructures are recommended to reduce sand sedimentation around the whole railway, notably downwind;

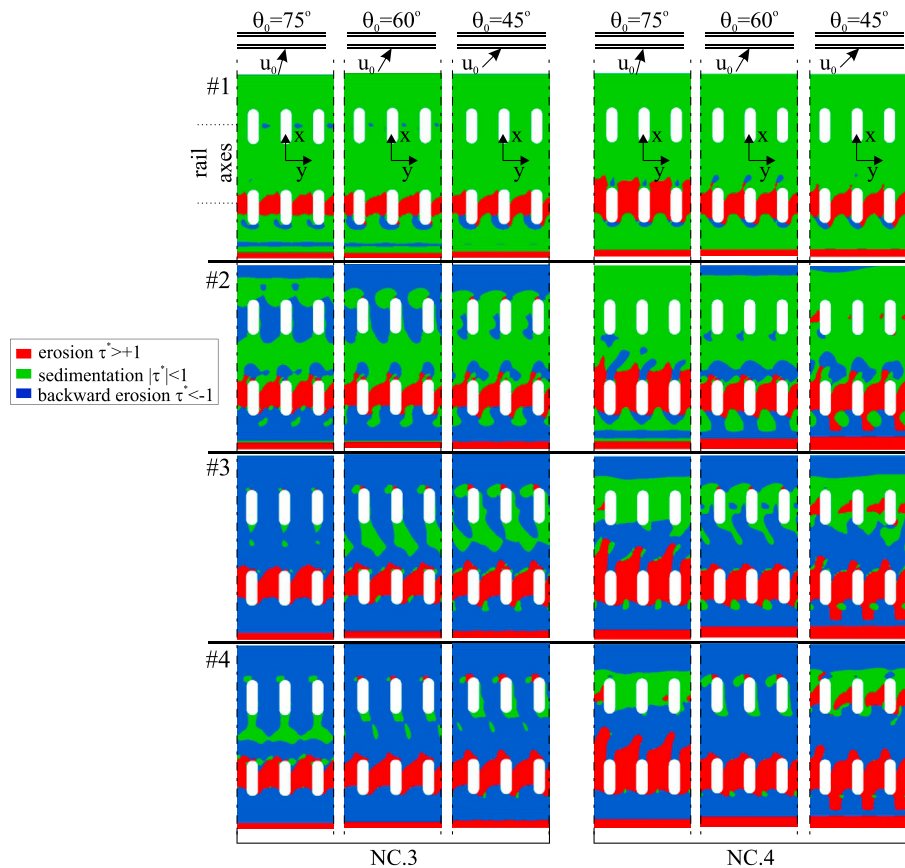


**Fig. 17.** Potential sedimentation, erosion and backward erosion patterns along non-conventional railway systems under differently yawed wind-flow (incoming wind from below).

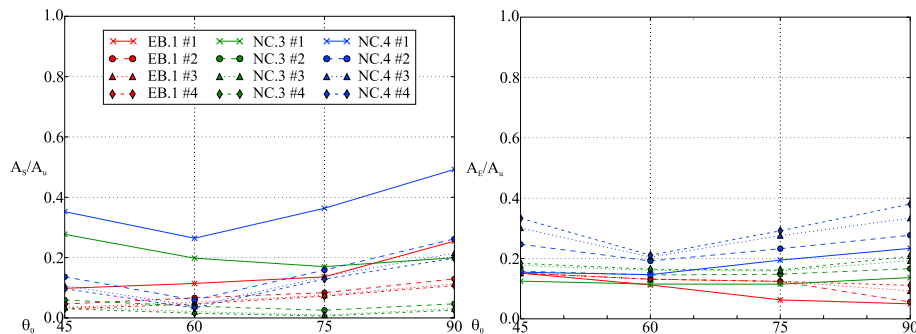


**Fig. 18.** Sedimentation (a) and erosion (b) normalized areas for selected cases under differently yawed wind-flow.

- large sedimentation and small erosion zones potentially occur around standard ballasted track system. Hence, alternative superstructures are needed in desert regions;
- track systems including humped sleepers/slab are promising solutions to promote sand erosion;
- the flow around humped sleepers/slab is strongly three-dimensional, very sensitive to the shape of the humps, and to the aerodynamic interaction with ballast bed, if present;
- accordingly, the erosion performances of humped sleepers/slab are affected by the above, by the yaw angle and speed of the incoming wind;
- in particular, the track system NC.4 shows the best erosion performances, but its sensitivity to wind yaw angle is critical for long railway lines exposed to trackwise variable wind regimes.

The study offers a well-defined framework for performance

assessment, and the obtained results introduce a solid phenomenological background. The adopted RANS-based computational model paves the way to the early stage, conceptual design of retrofitting measures for existing track systems, or of innovative track components for desert railways, possibly integrated by effective Receiver SMM(s) intended to further promote sand erosion on the track surface. More accurate approaches to the performance assessment of track and receiver SMM are still to be developed to meet the engineering needs during detailed and as-built design. These tools include, among others: i. more sophisticated, unsteady CFD simulations by LES able to predict sedimentation/erosion intermittency, as recently proposed by Brito et al. (2020); ii. multiphase wind-sand computational models able to simulate the dynamics of wind, saltating sand and sand accumulation/erosion profile, as reviewed in Lo Giudice et al. (2019) and applied in Lo Giudice and Preziosi (2020); iii. high-quality, well-documented WT tests fulfilling similarity requirements about railway embankment and track system, barrier, wind and sand

saltation layer, to be used for final verification and CWE validation; iv. accurate and robust measurement techniques to be adopted during long-term field trials.

### CRediT authorship contribution statement

**Marko Horvat:** Conceptualization, Methodology, Formal analysis, Writing - original draft, Writing - review & editing. **Luca Bruno:** Conceptualization, Methodology, Writing - original draft, Writing - review & editing. **Sami Khris:** Conceptualization, Methodology.

### Declaration of competing interest

The authors declare that they have no known competing financial interests or personal relationships that could have appeared to influence the work reported in this paper.

### Acknowledgments

The study has been funded by the European Union within the MSCA-ITN-2016-EID research project Sand Mitigation around Railway Tracks (SMaRT, [www.smart-eid.eu](http://www.smart-eid.eu)). The SMaRT project has received funding from the European Union Horizon 2020 research and innovation program under grant agreement No 721798. The Authors warmly acknowledge R. Sorge, P. Paoloni, P. Polidori, A. Ghezzi and F. Genta at Astaldi Company, SMaRT partner organization, who made possible the site visits along desert railways in Algeria and Iran. The kind availability of G. Wiggs and C. Nash is sharing their pictures along the Namibian railways is acknowledged as well. The study has been developed in the framework of the Windblown Sand Modelling and Mitigation (WSMM) joint research, development and consulting group established between Politecnico di Torino and Optiflow Company. Computational resources were provided by Optiflow Company and by HPC@POLITO, a project of Academic Computing within the Department of Control and Computer Engineering at the Politecnico di Torino (<http://www.hpc.polito.it>).

### References

- Araújo, A.D., Parteli, E.J.R., Pöschel, T., Andrade, J.S., Herrmann, H.J., 2013. Numerical modeling of the wind flow over a transverse dune. *Nature Sci. Rep.* 3.
- Bagnold, R., 1941. The Physics of Blown Sand and Desert Dunes. Methuen. <https://doi.org/10.1007/978-94-009-5682-7>.
- Baker, C., 1985. The determination of topographical exposure factors for railway embankments. *J. Wind Eng. Ind. Aerod.* 21, 89–99.
- Baker, C., 1986. Train aerodynamic forces and moments from moving model experiments. *J. Wind Eng. Ind. Aerod.* 24, 227–251.
- Bauer, B., Davidson-Arnott, R., Walker, I., Hesp, P.J.O., 2012. Wind direction and complex sediment transport response across a beach-dune system. *Earth Surf. Process. Landforms* 37, 1661–1677. <https://doi.org/10.1002/esp.3306>.
- Bauer, B., Walker, I., Baas, A., Jackson, D., Neuman, C., Wiggs, G., Hesp, P., 2013. Critical Reflections on the Coherent Flow Structures Paradigm in Aeolian Geomorphology, pp. 111–134. <https://doi.org/10.1002/9781118527221.ch8>.
- Blocken, B., Carmeliet, J., Stathopoulos, T., 2007. Cfd evaluation of wind speed conditions in passages between parallel buildings - effect of wall-function roughness modifications for the atmospheric boundary layer flow. *J. Wind Eng. Ind. Aerod.* 95, 941–962.
- Boccione, M., Cheli, F., Corradi, R., Muggiasca, S., Tomasini, G., 2008. Crosswind action on rail vehicles: wind tunnel experimental analyses. *J. Wind Eng. Ind. Aerod.* 96, 584–610.
- Bowen, A., 1983. The prediction of mean wind speeds above simple 2d hill shapes. *J. Wind Eng. Ind. Aerod.* 15, 259–270.
- Bowen, A., Lindley, D., 1977. A wind tunnel investigation of the wind speed and turbulence characteristics close to the ground over various escarpment shapes. *Boundary-Layer Meteorol.* 12, 259–271.
- Boyin, Z., Zhenhan, N., Qiankang, Z., Houxiang, W., 1992. A research on wind erosion simulation test on railway embankment in surface layer. *J. Wind Eng. Ind. Aerod.* 44, 2699–2700. [https://doi.org/10.1016/0167-6105\(92\)90062-F](https://doi.org/10.1016/0167-6105(92)90062-F).
- Brito, P.M., Ferreira, A.D., Thiis, T., Sousa, A.C.M., 2020. Prediction of erosion intermittency using large eddy simulation. *Geomorphology* 364, 107179. <https://doi.org/10.1016/j.geomorph.2020.107179>.
- Bruno, L., Fransos, D., 2015. Sand transverse dune aerodynamic: 3d coherent flow structures from a computational study. *J. Wind Eng. Ind. Aerod.* 147, 291–301. <https://doi.org/10.1016/j.jweia.2015.07.014>.
- Bruno, L., Fransos, D., Lo Giudice, A., 2018a. Solid barriers for windblown sand mitigation: aerodynamic behavior and conceptual design guidelines. *J. Wind Eng. Ind. Aerod.* 173, 79–90. <https://doi.org/10.1016/j.jweia.2017.12.005>.
- Bruno, L., Horvat, M., Raffaele, L., 2018b. Windblown sand along railway infrastructures: a review of challenges and mitigation measures. *J. Wind Eng. Ind. Aerod.* 177, 340–365. <https://doi.org/10.1016/j.jweia.2018.04.021>.
- Cabral, B., Leedom, L.C., 1993. Imaging vector fields using line integral convolution. In: SIGGRAPH '93. ACM Press, New York, New York, USA, pp. 263–270. <https://doi.org/10.1145/166117.166151>.
- Cebeci, T., Bradshaw, P., 1977. Momentum Transfer in Boundary Layers. Wash DC Hemisphere Publ Corp N Y McGraw-Hill Book Co.
- Cheli, F., Corradi, R., Rocchi, D., Tomasini, G., Maestrini, E., 2010. Wind tunnel tests on train scale models to investigate the effect of infrastructure scenario. *J. Wind Eng. Ind. Aerod.* 98, 353–362.
- Choi, H., Jeon, W.P., Kim, J., 2008. Control of flow over a bluff body. *Annu. Rev. Fluid Mech.* 40, 113–139. <https://doi.org/10.1146/annurev.fluid.39.050905.110149>.
- Deaves, D.M., 1980. Computations of wind flow over two-dimensional hills and embankments. *J. Wind Eng. Ind. Aerod.* 6, 89–111. [https://doi.org/10.1016/0167-6105\(80\)90024-0](https://doi.org/10.1016/0167-6105(80)90024-0).
- Delgado-Fernandez, I., Jackson, D.W.T., Cooper, J.A.G., Baas, A.C.W., Beyers, J.H.M., Lynch, K., 2013. Field characterization of three-dimensional lee-side airflow patterns under offshore winds at a beach-dune system. *J. Geophys. Res.-Earth* 118, 706–721. <https://doi.org/10.1002/jgrf.20036>.
- Demartino, C., Ricciardelli, F., 2017. Aerodynamics of nominally circular cylinders: a review of experimental results for civil engineering applications. *Eng. Struct.* 137, 76–114. <https://doi.org/10.1016/j.engstruct.2017.01.023>.
- Diedrichs, B., Sima, M., Orellano, A., Tengstrand, H., 2007. Crosswind stability of a high-speed train on a high embankment. *Proc. Inst. Mech. Eng. - Part F J. Rail Rapid Transit* 221, 205–225.
- Eurocode1, 2005. Actions on structures - part 1-4: General actions - wind actions - en 1991-1-4.
- Hesp, A.P., Smyth, T.A.G., 2019. Cfd flow dynamics over model scarps and slopes. *Phys. Geogr.* <https://doi.org/10.1080/02723646.2019.1706215>.
- Hesp, P., Smyth, T., Nielsen, P., Walker, I., Bauer, B., Davidson-Arnott, R., 2015. Flow deflection over a foredune. *Geomorphology* 230, 64–74. <https://doi.org/10.1016/j.geomorph.2014.11.005>.
- Horvat, M., Bruno, L., Khris, S., Raffaele, L., 2020. Aerodynamic shape optimization of barriers for windblown sand mitigation using cfd analysis. *J. Wind Eng. Ind. Aerod.* 197 <https://doi.org/10.1016/j.jweia.2019.104058>.
- Ishak, I., Ali, M., Sakri, F., Zulkifli, F., Darlis, N., Mahmudin, R., Abidin, S., Azizul, M., Sulaiman, S., Samiran, N., Khalid, A., 2019. Aerodynamic characteristics around a generic train moving on different embankments under the influence of crosswind. *Journal of Advanced Research in Fluid Mechanics and Thermal Sciences* 61, 117–139.
- Jackson, D.W.T., Beyers, J.H.M., Lynch, K., Cooper, J.A.G., Baas, A.C.W., Delgado-Fernandez, I., 2011. Investigation of three-dimensional wind flow behaviour over coastal dune morphology under offshore winds using computational fluid dynamics (CFD) and ultrasonic anemometry. *Earth Surf. Process. Landforms* 36, 1113–1124.
- Jackson, D.W.T., Beyers, J.H.M., Delgado-Fernandez, I., Baas, A.C.W., Cooper, J.A.G., Lynch, K., 2013. Airflow reversal and alternating corkscrew vortices in foredune wake zones during perpendicular and oblique offshore winds. *Geomorphology* 187, 86–93.
- Kim, W., Choi, H., 2019. Effect of the spanwise computational domain size on the flow over a two-dimensional bluff body with spanwise periodic perturbations at low Reynolds number. *Comput. Fluid* 183, 102–106. <https://doi.org/10.1016/j.compfluid.2019.01.006>.
- Launder, B.E., Spalding, D.B., 1974. The numerical computation of turbulent flows. *Comput. Methods Appl. Mech. Eng.* 3, 269–289.
- Lima, I., Araújo, A., Parteli, E.J.R., Herrmann, H.J., 2017. Optimal array of sand fences. *Sci. Rep.* 7 <https://doi.org/10.1038/srep45148>.
- Liu, B., Qu, J., Zhang, W., Qian, G., 2011. Numerical simulation of wind flow over transverse and pyramid dunes. *J. Wind Eng. Ind. Aerod.* 99, 879.
- Lo Giudice, A., Preziosi, L., 2020. A fully eulerian multiphase model of windblown sand coupled with morphodynamic evolution: erosion, transport, deposition, and avalanching. *Appl. Math. Model.* 79, 68–84. <https://doi.org/10.1016/j.apm.2019.07.060>.
- Lo Giudice, A., Nuca, R., Preziosi, L., Coste, N., 2019. Wind-blown particulate transport: a review of computational fluid dynamics models. *Mathematics in Engineering* 1, 508–547. <https://doi.org/10.3934/MINE.2019.3.508>.
- Menter, F.R., 1994. Two-equation eddy-viscosity turbulence models for engineering applications. *AIAA J.* 32, 269–289. <https://doi.org/10.2514/3.12149>.
- Menter, F.R., Kuntz, M., Langtry, R., 2003. Ten years of industrial experience with the SST turbulence model. In: Hanjalić, K., Nagano, Y., Tummers, J. (Eds.), *Turbulence Heat and Mass Transfer 4: Proceedings of the Fourth International Symposium on Turbulence, Heat and Mass Transfer*, Antalya, Turkey, 12–17 October, 2003. Begell House, p. 1208.
- Merino, P., 2014. Arabia saudi: un reto exigente para la internacionalización de la tecnología española. *Lineas* 80, 58–67. URL: [http://www.adif.es/es\\_ES/comunicacion\\_y\\_prensa/doc/UltimoNumero.pdf](http://www.adif.es/es_ES/comunicacion_y_prensa/doc/UltimoNumero.pdf).
- Moyan, Z., Hong, X., Nadakatti, M.M., Feng, J., Guangpeng, L., 2020. Track structure failure caused by sand deposition: simulation and experimentation. *Aeolian Research* 43. <https://doi.org/10.1016/j.aeolia.2020.100578>.
- Noguchi, Y., Suzuki, M., Baker, C., Nakade, K., 2019. Numerical and experimental study on the aerodynamic force coefficients of railway vehicles on an embankment in crosswind. *J. Wind Eng. Ind. Aerod.* 184, 90–105. <https://doi.org/10.1016/j.jweia.2018.11.019>.

- Paterson, D.A., Holmes, J.D., 1993. Computation of wind flow over topography. *J. Wind Eng. Ind. Aerod.* 46–47, 471–476. [https://doi.org/10.1016/0167-6105\(93\)90314-E](https://doi.org/10.1016/0167-6105(93)90314-E).
- Raffaele, L., Bruno, L., 2019. Windblown sand action on civil structures: definition and probabilistic modelling. *Eng. Struct.* 178, 88–101. <https://doi.org/10.1016/j.engstruct.2018.10.017>.
- Raffaele, L., Bruno, L., Pellecerry, F., Preziosi, L., 2016. Windblown sand saltation: a statistical approach to fluid threshold shear velocity. *Aeolian Research* 23, 79–91. <https://doi.org/10.1016/j.aeolia.2016.10.002>.
- Reissberger, K., Guggenberger, E., Ossberger, H., 2016. Sleepers having elevated rail fastening as protection against sand coverage. URL. <https://patents.google.com/patent/EP2984230A1>.
- Richards, P., Norris, S., 2011. Appropriate boundary conditions for computational wind engineering models revisited. *J. Wind Eng. Ind. Aerod.* 99, 257–266.
- Reissberger, K., 2015. Heavy haul in sand environment. In: IHHA 2015 Conference, Perth, Australia. URL [http://railknowledgebank.com/Presto/content/GetDoc.axd?ctID=MTk4MTRjNDUtNWQ0My00TBmLTlIYWUtZWFM2U2OTE0ZDY3&ID=MjgyOQ==&ID=Nz克斯&attachmnt=VHJ1ZQ==&uSesDM=False&rldx=Mjg4OA==&prCFU=](http://railknowledgebank.com/Presto/content/GetDoc.axd?ctID=MTk4MTRjNDUtNWQ0My00TBmLTlIYWUtZWFM2U2OTE0ZDY3&ID=MjgyOQ==&ID=Nzкс&attachmnt=VHJ1ZQ==&uSesDM=False&rldx=Mjg4OA==&prCFU=).
- Reissberger, K., Swanepoel, W., 2005. Specialised sleepers combat sand. *Railw. Gaz. Int.* 55URL. <https://trid.trb.org/view.aspx?id=789500>.
- Schlichting, H., 1979. *Boundary-layer Theory*. McGraw-Hill.
- Schober, M., Weise, M., Orellano, A., Deeg, P., Wetzel, W., 2010. Wind tunnel investigation of an ice 3 endcar on three standard ground scenarios. *J. Wind Eng. Ind. Aerod.* 98, 345–352. <https://doi.org/10.1016/j.jweia.2009.12.004>.
- Shiau, B., Hsieh, C., 2002. Wind flow characteristics and Reynolds stress structure around the two-dimensional embankment of trapezoidal shape with different slope gradients. *J. Wind Eng. Ind. Aerod.* 90, 1645–1656. [https://doi.org/10.1016/S0167-6105\(02\)00276-3](https://doi.org/10.1016/S0167-6105(02)00276-3).
- Smyth, T., 2016. A review of computational fluid dynamics (cfd) airflow modelling over aeolian landforms. *Aeolian Research* 22, 153–164. <https://doi.org/10.1016/j.aeolia.2016.07.003>.
- Suzuki, M., Tanemoto, K., Maeda, T., 2003. Aerodynamic characteristics of train/vehicles under cross winds. *J. Wind Eng. Ind. Aerod.* 91, 209–218. [https://doi.org/10.1016/S0167-6105\(02\)00346-X](https://doi.org/10.1016/S0167-6105(02)00346-X).
- Sweby, P.K., 1984. High resolution schemes using flux limiters for hyperbolic conservation laws. *SIAM J. Numer. Anal.* 21, 995–1011. URL. <https://www.jstor.org/stable/2156939>.
- Sweet, M., Kocurek, G., 1990. An empirical model of aeolian dune lee-face airflow. *Sedimentology* 37, 1023–1038. <https://doi.org/10.1111/j.1365-3091.1990.tb01843.x>.
- Tomasini, G., Giappino, S., Corradi, R., 2014. Experimental investigation of the effects of embankment scenario on railway vehicle aerodynamic coefficients. *J. Wind Eng. Ind. Aerod.* 131, 59–71. <https://doi.org/10.1016/j.jweia.2014.05.004>.
- van der Merwe, J., 2013. T-track system. URL. <http://ttracksaudi.com>.
- Walker, I.J., Nickling, W.G., 2002. Dynamics of secondary airflow and sediment transport over and in the lee of transverse dunes. *Prog. Phys. Geogr.* 26, 47–75. <https://doi.org/10.1191/0309133302pp325ra>.
- Walker, I., Hesp, P., Davidson-Arnott, R.J.O., 2006. Topographic steering of alongshore airflow over a vegetated foredune: greenwich dunes, prince edward island, Canada. *J. Coast Res.* 22, 1278–1291. <https://doi.org/10.2112/06A-0010.1>.
- Xiao, J., Yao, Z., Qu, J., 2015. Influence of golmud-lhasa section of qinghai-tibet railway on blown sand transport. *Chin. Geogr. Sci.* 25, 39–50. <https://doi.org/10.1007/s11769-014-0722-1>.
- Zakeri, J.A., 2012. Investigation on railway track maintenance in sandy-dry areas. *Struct. Infrastruct. Eng. Maint., Manag. Life-Cycle Des. Perform.* 8, 135–140. <https://doi.org/10.1080/15732470903384921>.
- Zakeri, J.A., Esmaeli, M., Fathali, M., 2011. Evaluation of humped slab track performance in desert railways. *Proc. Inst. Mech. Eng. - Part F J. Rail Rapid Transit* 225, 566–573. <https://doi.org/10.1177/0954409711403677>.
- Zakeri, J.A., Esmaeli, M., Mosayebi, S., Abbasi, R., 2012. Effects of vibration in desert area caused by moving trains. *Journal of Modern Transportation* 20, 16–23. <https://doi.org/10.1007/BF03325772>.
- Zhang, J., Cui, E., Fu, G., 1995. Investigation of the flow field and the starting conditions of wind-induced erosion of the railway embankment. *J. Wind Eng. Ind. Aerod.* 54–55, 573–581. [https://doi.org/10.1016/0167-6105\(94\)00073-M](https://doi.org/10.1016/0167-6105(94)00073-M).
- Zhang, J., Wang, J., Tan, X., Gao, G., Xiong, X., 2019. Detached eddy simulation of flow characteristics around railway embankments and the layout of anemometers. *J. Wind Eng. Ind. Aerod.* 193 <https://doi.org/10.1016/j.jweia.2019.103968>.